Time-Averaged Model for Irregular Breaking Waves on Porous Structures and Beaches

by

Leslie Elizabeth Meigs and Nobuhisa Kobayashi

RESEARCH REPORT NO. CACR-04-02
October, 2004

Center for Applied Coastal Research
Ocean Engineering Laboratory
University of Delaware
Newark, DE 19716

ACKNOWLEDGEMENTS

During my time at Delaware, my advisor Nobuhisa Kobayashi has been helpful as both an advisor and mentor. I truly appreciate his candor and expertise in classwork, research, and career advisement. I would also like to thank Maryland Materials in Northeast, Maryland for helping me with the selection of stones and the usage of their space during the first and second sorting of the stones. Jeffrey Melby of the Coastal and Hydraulics Laboratory at the Waterways Experiments Station in Vicksburg, MS has also been of great support. Thanks also to Dr. Takao Ota of Tottori University in Japan who, during his time at Delaware as a visiting professor, taught me how to use the flume as well as build the stone breakwater.

This study was supported by the U.S. Army Corps of Engineers, Coastal and Hydraulics Laboratory under Contract Number DACW42-03-C-0024.

TABLE OF CONTENTS

LIST OF FIGURES iii
LIST OF TABLES vi
ABSTRACT vii

Chapter

1 INTRODUCTION 1

2 IRREGULAR BREAKING WAVE TRANSMISSION OVER SUBMERGED POROUS BREAKWATER 4

2.1 Introduction 4
2.2 Experiment 5

2.2.1 Experimental Setup 5
2.2.2 Stone Characteristics 7
2.2.3 Free Surface and Velocity Measurements 16

2.3 Numerical Model 28
2.4 Comparison Between Experiments and Numerical Model 41

3 IRREGULAR BREAKING WAVE TRANSFORMATION ON POROUS REVETMENT 57

3.1 Introduction 57
3.2 Time-Dependent Numerical Model PBREAK 57
3.3 Comparison with Time-Dependent Model 59

4 CONCLUSIONS 75

REFERENCES 77

LIST OF FIGURES

2.1 Experimental Setup with Water Depth d_c = 4, 6, 8 and 10 cm Above Submerged Breakwater 6

2.2 Cross-shore Locations of Eight Wave Gauges and Three Acoustic Doppler Velocimeters 7

2.3 % Finer by Mass for Stone Sets One and Two 15

2.4 Calibration Curve for Wave Gauge 1 17

2.5 Measured Cross-Shore Variations of Mean Free Surface Elevation, $\overline{\eta}$ 22

2.6 Measured Cross-Shore Variations of Standard Deviation of Free Surface Elevation, σ_η 24

2.7 Measured Cross-Shore Variations of Mean Horizontal Velocity , $\overline{u}$ 26

2.8 Measured Cross-Shore Variations of Standard Deviation of Horizontal Velocity, σ_u 27

2.9 Functions G_2 and G_3 and Fitted Equations 31

2.10 Dimensionless Coefficient, C_v 37

2.11 Measured and Computed Cross-Shore Variations of Mean and Standard Deviation of η and u Above Bottom Profile, z_b, for Test R6 with Slope Adjustment Factor b = 3 and 2 47

2.12 Computed Cross-Shore Variations of Wave Shoaling and Breaking Parameters n, a, Q, and σ_* 48

2.13 Computed Cross-Shore Variations of Radiation Stress, $S_{xx} = \rho g S^*_{xx}$, and Bottom Shear Stress, $\tau_b = \rho g \tau^*_b$ 49

2.14 Computed Cross-Shore Variations of Mean and Standard Deviation of Horizontal Discharge Velocity, v, Inside Porous Breakwater 49

2.15 Computed Cross-Shore Variations of Wave Energy Flux, $F = \rho g F^*$, and Dissipation Rates, $D_B = \rho g D_B^*$, $D_r = \rho g D_r^*$, and $D_f = \rho g D_f^*$, Due to Wave Breaking, Porous Flow Resistance, and Bottom Friction, Respectively 50

2.16 Sensitivity to Bottom Friction Factor, $f_b = 0.01$ and 0.05 51

2.17 Sensitivity to Turbulent Porous Flow Resistance Factor, $\beta_0 = 5$ and 1 52

2.18 Sensitivity to Breaker Ratio Parameter, $\gamma = 0.7$ and 0.6, for Test R6 53

2.19 Comparison with Data for Test R4 54

2.20 Comparison with Data for Test R8 55

2.21 Comparison with Data for Test R10 56

3.1 Comparisons of Mean and Standard Deviation of Free Surface Elevation, η, Horizontal Fluid Velocity, u, and Horizontal Discharge Velocity, v, Inside Porous Layer for Test P2 Along with Upper and Lower Boundaries of Porous Layer 61

3.2 Cross-Shore Variations of Wave Shoaling and Breaking Parameters n, a and Q Computed by Time-Averaged Model CSHOREP for Test P2 62

3.3 Cross-Shore Variations of Radiation Stress, $S_{xx} = \rho g S_{xx}^*$, and Bottom Shear Stress, $\tau_b = \rho g \tau_b^*$, Computed by CSHOREP for Test P2 63

3.4 Cross-Shore Variations of Wave Energy Flux, $F = \rho g F^*$, and Dissipation Rates, $D_B = \rho g D_B^*$, $D_r = \rho g D_r^*$, and $D_f = \rho g D_f^*$, Due to Wave Breaking, Porous Flow Resistance, and Bottom Friction, Respectively, Computed by CSHOREP for Test P2 65

3.5 Comparisons of Mean and Standard Deviation of Free Surface Elevation, η, Horizontal Fluid Velocity, u, and Horizontal Discharge Velocity, v, Inside Porous Layer for Test P1 Along with Upper and Lower Boundaries of Porous Layer Between CSHOREP and PBREAK.....67

3.6 Cross-Shore Variations of Wave Shoaling and Breaking Parameters n, a and Q Computed by CSHOREP for Test P1 68

3.7 Cross-Shore Variations of Radiation Stress, $S_{xx} = \rho g S_{xx}^*$, and Bottom Shear Stress, $\tau_b = \rho g \tau_b^*$, Computed by CSHOREP for Test P1 69

3.8 Cross-Shore Variations of Wave Energy Flux, $F = \rho g F^*$, and Dissipation Rates, $D_B = \rho g D_B^*$, $D_r = \rho g D_r^*$, and $D_f = \rho g D_f^*$, Due to Wave Breaking, Porous Flow Resistance, and Bottom Friction, Respectively, Computed by CSHOREP for Test P1 70

3.9 Comparisons of Mean and Standard Deviation of Free Surface Elevation, η, Horizontal Fluid Velocity, u, and Horizontal Discharge Velocity, v, Inside Porous Layer for Test P3 Along with Upper and Lower Boundaries of Porous Layer Between CSHOREP and PBREAK.....71

3.10 Cross-Shore Variations of Wave Shoaling and Breaking Parameters n, a and Q Computed by CSHOREP for Test P3 72

3.11 Cross-Shore Variations of Radiation Stress, $S_{xx} = \rho g S_{xx}^*$, and Bottom Shear Stress, $\tau_b = \rho g \tau_b^*$, Computed by CSHOREP for Test P3 73

3.12 Cross-Shore Variations of Wave Energy Flux, $F = \rho g F^*$, and Dissipation Rates, $D_B = \rho g D_B^*$, $D_r = \rho g D_r^*$, and $D_f = \rho g D_f^*$, Due to Wave Breaking, Porous Flow Resistance, and Bottom Friction, Respectively, Computed by CSHOREP for Test P3 74

LIST OF TABLES

2.1 Stone Characteristics for Stone Sample Set One 9

2.2 Stone Characteristics for Stone Sample Set Two 12

2.3 Still Water Depth at Gauge Locations 16

2.4 Measured Wave Characteristics at Wave Gauge 1 18

2.5 Measured Mean Free Surface Elevation, $\bar{\eta}$ (cm) 21

2.6 Standard Deviation of the Free Surface Elevation, σ_η (cm) 23

2.8 Mean and Standard Deviation of Horizontal Velocity (cm/s) at x = 5.008, 6.108, and 7.158 m.....25

3.1 Input to Time-Averaged Model 59

ABSTRACT

A numerical model based on time-averaged continuity, momentum and energy equations is developed to predict the mean and standard deviation of the free surface elevation and horizontal fluid velocities above and inside a porous submerged breakwater. The energy dissipation rate due to irregular breaking waves is estimated using an existing formula that is modified for intense wave breaking on the steep seaward slope of the breakwater. The developed model is shown to predict the cross-shore variations of the mean and standard deviation of the free surface elevation and horizontal velocity measured in a laboratory experiment where a submerged porous breakwater was placed on a gentle impermeable slope. In addition the time-averaged model is compared with the corresponding time-dependent model which was verified using three tests for irregular wave runup on a 1/3 slope with a thick porous layer. The cross-shore variations of the mean and standard deviation of the free surface elevation and fluid velocities computed by the two models are shown to be in agreement for the three tests. The time-averaged model reduces the computation time by a factor of 10^{-3} and requires only the offshore wave data which is normally available.

CHAPTER 1

INTRODUCTION

Irregular wave breaking and wave setup on an impermeable beach of an arbitrary profile are normally predicted using numerical models such as that of Battjes and Stive (1985)

based on time-averaged momentum and energy equations. The time-averaged models predict only the mean and standard deviation of the free surface elevation but are widely used because of its computational efficiency. However, the existing time-averaged model cannot be applied to an impermeable beach with a rubble-mound structure. Furthermore, no time-averaged model exists for permeable beaches such as gravel and cobble beaches.

Cobble beaches are poorly understood in comparison to conventional rubble mound breakwaters and sand beaches. Cobble and gravel beaches may not be as common as sand beaches but do exist along some coasts. A dynamic revetment that resembles a natural cobble beach was constructed for the protection of an eroding sand beach (Allan and Komar 2002). The cobble revetment is dynamic because of the movement of cobbles by waves and currents during storms in contrast to conventional

stone revetments that are designed for the static stability of stones. The slopes of cobble beaches and revetments are gentler than berm breakwaters (e.g., Sigurdarson et al. 2001) and berm revetments (Ahrens and Ward 1991). Cobble beaches and structures are not discussed in textbooks on coastal processes and structures.

On the other hand, breaking wave transformation on porous structures and beaches is predicted using various numerical models based on time-dependent continuity and momentum equations as discussed by Kobayashi and Wurjanto (1990), Cruz et al. (1992), Wurjanto and Kobayashi (1993), van Gent (1994), Liu et al. (1999), Méndez et al. (2001), and Clarke et al. (2004). The time-dependent models predict the time series of the free surface elevation and fluid velocities but require significant efforts to compute the rapid variations of breaking waves. Consequently, these models are not adopted widely for practical applications. The difficulties in the development of the corresponding time-averaged models include a closure problem where the time averaging of the governing equations results in more unknown variables than the number of equations. In addition, no formula is available to estimate the time-averaged rate of energy dissipation due to wave breaking on the structure. These difficulties are addressed in the time-averaged model developed in Chapter 2.

The knowledge of waves and currents on permeable bottoms is essential to predict the evolutions of cobble beaches and revetments under irregular breaking waves. Time-dependent numerical models for breaking waves on permeable structures [e.g., Wurjanto and Kobayashi (1993)] were developed to predict the detailed wave motions on relatively steep slopes for a short duration as discussed in Chapter 3. These models require

significant computation time and are not suited for the prediction of the profile changes of cobble beaches and revetments under sequences of storms. The time-averaged numerical model developed in Chapter 2 is compared in Chapter 3 with the corresponding time-dependent model of Wurjanto and Kobayashi (1993) who showed that their model could predict irregular wave runup on a porous revetment.

It is noted that the summary of Chapter 2 has been submitted to the Journal of Waterway, Port and Coastal Engineering (Kobayashi, Meigs, Ota and Melby, 2004). Chapter 3 will be published in the Proceedings of the 29th International Conference on Coastal Engineering (Meigs, Kobayashi and Melby, 2004).

CHAPTER 2

IRREGULAR BREAKING WAVE TRANSMISSION OVER SUBMERGED POROUS BREAKWATER

2.1 INTRODUCTION

The specific problem examined hereafter is irregular wave transmission over a submerged porous breakwater situated in the surf zone on a beach. Submerged breakwaters are widely used for shoreline protection in some countries because of their aesthetics and effectiveness in triggering wave breaking without eliminating the landward flow of water, which may be important for water quality considerations [e.g., Kobayashi and Wurjanto (1989)].

A submerged stone breakwater was constructed on a gentle impermeable slope and exposed to irregular breaking waves. Measurements were made of the free surface elevations and fluid velocities for the calibration and verification of the developed time-averaged model.

In the following, the experiment is presented first because it is easier to explain the effects of the structure on wave breaking using the experimental observations. Second, a time-averaged model is derived from the continuity, momentum and energy equations in shallow water. Third, the time-averaged model is compared with the

measurements and the sensitivities of the computed results to four empirical parameters are discussed. Finally, the findings of this study are summarized along with possible future work.

2.2 EXPERIMENT

2.2.1 EXPERIMENTAL SETUP

An experiment was conducted in a wave flume with glass side walls that was 33 m long, 0.6 m wide and 1.5 m high as shown in Figure 2.1. An impermeable beach with a 1/35 slope was constructed of a smooth solid material used for kitchen countertops. A submerged breakwater was constructed of angular stone on the 1/35 slope.

The seaward and landward slopes of the breakwater were 1/2.28 and 1/1.40, respectively. The width of the horizontal crest of the breakwater was 164 cm, that is, 48 D_{n50} and much wider than the crest width of a conventional low-crested rubble mound structure (van der Meer and Daemen 1994) and a reef breakwater (Ahrens 1989). The geometry of the model breakwater in Figure 2.1 was approximately based on the *Artificial reef design manual* (1992) in Japan. The still water depth, d_c, on the crest is required to be large enough to avoid ship collision. The wide crest is then necessary to reduce wave transmission.

Four tests R4, R6, R8 and R10 were performed for the wide reef with d_c = 4, 6, 8 and 10 cm where the numeral after the letter R corresponds to the value of d_c. Irregular waves, based on the TMA spectrum, were generated using a piston-type wave paddle. The spectral peak period was T_p = 2.32 s. The root-mean-square wave height, H_{rms},

defined as $H_{rms} = \sqrt{8}\,\sigma_\eta$, with σ_η = standard deviation of the free surface elevation η, was chosen to generate large waves without any wave breaking in the region of the still water depth, d_h, on the horizontal bottom in Figure 2.1. Eight wave gauges and three acoustic Doppler velocimeters (ADV) were deployed as shown in Figure 2.2 where the cross-shore coordinate, x, positive onshore with $x = 0$ at wave gauge 1, is used subsequently to indicate the cross-shore location of each measurement. The vertical coordinate, z, is positive upward with $z = 0$ at the still water level (SWL) as shown in Figure 2.1. The still water depth at $x = 0$ was $(d_c + 30.9)$ cm. It should be noted that a small gap at the toe of the 1/35 slope was sealed using the breakwater stone. Consequently, only the region of $x \geq 0$ is considered in the following.

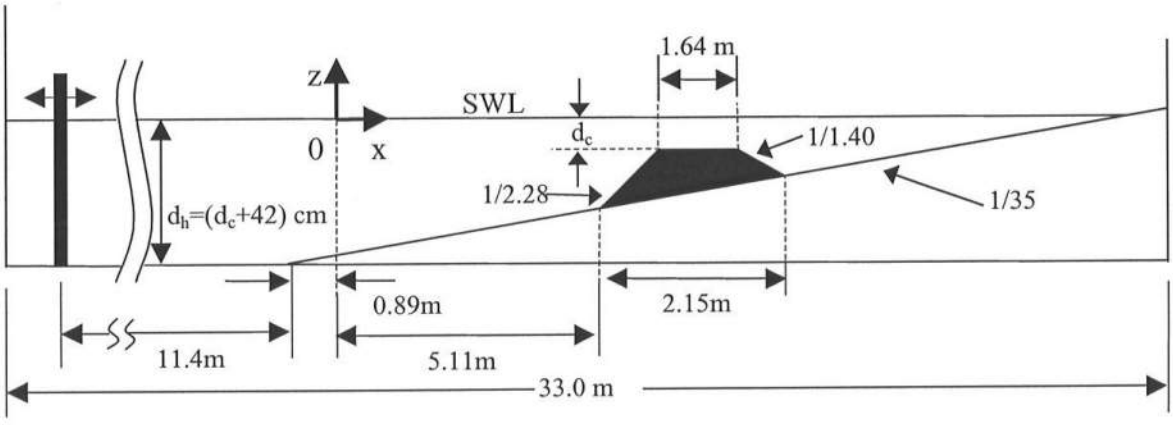

Figure 2.1: Experimental Setup with Water Depth d_c = 4, 6, 8 and 10 cm Above Submerged Breakwater

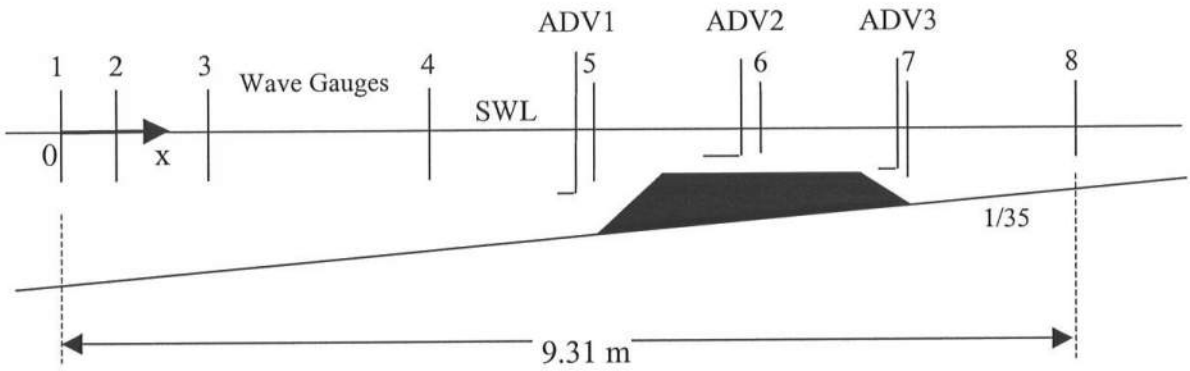

Figure 2.2: Cross-Shore Locations of Eight Wave Gauges and Three Acoustic Doppler Velocimeters

2.2.2 STONE CHARACTERISTICS

Since the breakwater would be subject to a variety of water depths and large waves, stones of sufficiently large size were chosen to resist movement. Mass, volume, density and percent finer by mass were determined for each stone for the sample set of 100 stones and another sample set of 100 stones. A second set of sample stones was used after it was determined that more stones would be needed to construct the breakwater and that the new stones must be of the same characteristics as the first sample set. The volume measurements represent the average volume after 10 measurements of the water volume displaced by each stone. The results for the stone characteristic analysis were tabulated and are presented in Table 2.1 and Table 2.2, for sample set one and two, respectively. From these results the median mass, M_{50} = 118.18 g was interpolated for both sets of stone samples. The % finer by mass comparison of set one and two can be

seen in Figure 2.3. Once the median mass was determined, the nominal diameter defined in Equation (2.1), was calculated

$$D_{n50} = (M_{50}/\rho_s)^{1/3} \tag{2.1}$$

where ρ_s = stone density. Using $\rho_s = 2.95$ g/cm^3 the nominal diameter was calculated as 3.4cm. Porosity of the structure was measured by weighing stones in a container of known mass and volume. The mass of the stones was noted and then water was added to the container until the container was filled. The mass of the container with water and stones was then measured. Knowing the density of the stones and water, the porosity of the structure was calculated as $n_p = 0.5$.

Table 2.1: Stone Characteristics for Stone Sample Set One

Stone	Mass (g)	Average Volume (cm3)	Density (g/cm3)	Cumulative Mass	% Finer by mass
S94	66.30	21.60	3.07	66.30	0.59
S97	67.70	24.40	2.77	134.00	1.20
S67	67.70	22.40	3.02	201.70	1.80
S18	68.10	21.20	3.21	269.80	2.41
S15	69.90	22.80	3.07	339.70	3.03
S38	70.80	25.00	2.83	410.50	3.67
S63	73.10	24.60	2.97	483.60	4.32
S99	75.80	27.20	2.79	559.40	5.00
S28	76.70	27.00	2.84	636.10	5.68
S54	77.20	27.60	2.80	713.30	6.37
S42	79.90	28.80	2.77	793.20	7.09
S62	81.70	26.60	3.07	874.90	7.81
S46	82.60	29.40	2.81	957.50	8.55
S70	82.60	29.60	2.79	1040.10	9.29
S41	83.50	27.80	3.00	1123.60	10.04
S90	84.50	28.60	2.95	1208.10	10.79
S56	85.40	29.80	2.87	1293.50	11.55
S66	86.30	30.00	2.88	1379.80	12.32
S82	86.30	29.00	2.98	1466.10	13.10
S30	86.70	30.00	2.89	1552.80	13.87
S59	88.10	28.20	3.12	1640.90	14.66
S2	88.50	30.20	2.93	1729.40	15.45
S69	89.00	31.60	2.82	1818.40	16.24
S92	90.80	29.60	3.07	1909.20	17.05
S80	92.60	30.60	3.03	2001.80	17.88
S68	93.10	30.00	3.10	2094.90	18.71
S48	94.90	29.80	3.18	2189.80	19.56
S3	95.30	30.40	3.13	2285.10	20.41
S79	95.80	30.80	3.11	2380.90	21.27
S57	97.60	30.00	3.25	2478.50	22.14
S72	99.40	33.20	2.99	2577.90	23.03
S17	101.30	30.60	3.31	2679.20	23.93
S32	102.60	34.60	2.97	2781.80	24.85
S40	103.50	34.40	3.01	2885.30	25.77
S39	104.00	33.20	3.13	2989.30	26.70
S60	104.00	39.00	2.67	3093.30	27.63

Table 2.1 continued: Stone Characteristics for Stone Sample Set One

Stone	Mass (g)	Average Volume (cm3)	Density (g/cm3)	Cumulative Mass	% Finer by mass
S43	104.90	34.40	3.05	3198.20	28.57
S50	104.90	37.80	2.78	3303.10	29.50
S64	104.90	35.20	2.98	3408.00	30.44
S33	105.30	35.60	2.96	3513.30	31.38
S85	105.80	37.20	2.84	3619.10	32.33
S13	106.70	34.40	3.10	3725.80	33.28
S23	107.20	38.20	2.81	3833.00	34.24
S55	107.60	38.60	2.79	3940.60	35.20
S76	108.50	38.80	2.80	4049.10	36.17
S26	109.40	35.40	3.09	4158.50	37.14
S53	109.90	40.00	2.75	4268.40	38.13
S88	110.30	34.80	3.17	4378.70	39.11
S75	110.30	40.00	2.76	4489.00	40.10
S12	110.80	39.60	2.80	4599.80	41.09
S6	111.70	39.20	2.85	4711.50	42.08
S8	111.70	36.60	3.05	4823.20	43.08
S22	111.70	35.80	3.12	4934.90	44.08
S96	113.10	39.40	2.87	5048.00	45.09
S19	115.80	38.60	3.00	5163.80	46.12
S65	115.80	39.40	2.94	5279.60	47.16
S49	116.70	38.80	3.01	5396.30	48.20
S34	118.00	40.80	2.89	5514.30	49.26
S100	118.50	39.40	3.01	5632.80	50.31
S37	118.50	40.00	2.96	5751.30	51.37
S29	118.50	39.80	2.98	5869.80	52.43
S61	118.50	38.20	3.10	5988.30	53.49
S95	119.00	40.80	2.92	6107.30	54.55
S35	119.00	43.20	2.75	6226.30	55.61
S73	120.30	39.40	3.05	6346.60	56.69
S16	120.80	40.00	3.02	6467.40	57.77
S14	120.80	41.20	2.93	6588.20	58.85
S81	120.80	40.40	2.99	6709.00	59.93
S11	121.20	40.00	3.03	6830.20	61.01
S78	122.10	39.60	3.08	6952.30	62.10
S71	123.50	42.20	2.93	7075.80	63.20
S51	124.40	39.20	3.17	7200.20	64.31

Table 2.1 continued: Stone Characteristics for Stone Sample Set One

Stone	Mass (g)	Average Volume (cm3)	Density (g/cm3)	Cumulative Mass	% Finer by mass
S86	125.30	44.60	2.81	7325.50	65.43
S36	125.80	44.40	2.83	7451.30	66.56
S58	126.70	39.80	3.18	7578.00	67.69
S44	129.40	40.60	3.19	7707.40	68.84
S84	131.20	47.00	2.79	7838.60	70.02
S7	131.70	40.40	3.26	7970.30	71.19
S83	134.80	45.00	3.00	8105.10	72.40
S93	135.30	45.00	3.01	8240.40	73.61
S1	136.20	46.60	2.92	8376.60	74.82
S21	138.50	47.60	2.91	8515.10	76.06
S87	138.50	45.00	3.08	8653.60	77.30
S25	139.40	49.60	2.81	8793.00	78.54
S47	141.70	49.80	2.85	8934.70	79.81
S45	143.00	50.40	2.84	9077.70	81.08
S89	143.50	47.80	3.00	9221.20	82.37
S91	145.30	52.00	2.79	9366.50	83.66
S27	146.20	45.80	3.19	9512.70	84.97
S52	146.70	45.20	3.25	9659.40	86.28
S10	148.50	49.20	3.02	9807.90	87.61
S74	150.30	50.20	2.99	9958.20	88.95
S9	150.70	53.40	2.82	10108.90	90.30
S4	151.60	50.20	3.02	10260.50	91.65
S5	151.60	50.00	3.03	10412.10	93.00
S31	152.60	51.60	2.96	10564.70	94.37
S98	155.30	56.40	2.75	10720.00	95.75
S20	156.20	52.40	2.98	10876.20	97.15
S77	159.40	55.20	2.89	11035.60	98.57
S24	159.80	51.60	3.10	11195.40	100.00
Total	11195.4	3778.4	296.803		
Average	111.95	37.78	2.97		

Table 2.2: Stone Characteristics for Stone Sample Set Two

Stone	Mass (g)	Average Volume (cm3)	Density (g/cm3)	Cumulative Mass	% Finer by mass
SS97	58.80	20.40	2.88	58.80	0.53
SS78	64.60	25.20	2.56	123.40	1.10
SS30	67.80	22.40	3.03	191.20	1.71
SS21	68.00	23.00	2.96	259.20	2.32
SS26	68.90	20.20	3.41	328.10	2.93
SS65	71.30	23.40	3.05	399.40	3.57
SS88	73.60	23.80	3.09	473.00	4.23
SS85	74.80	47.00	1.59	547.80	4.90
SS71	75.90	27.80	2.73	623.70	5.57
SS54	77.10	27.40	2.81	700.80	6.26
SS80	79.80	27.40	2.91	780.60	6.98
SS53	80.40	27.80	2.89	861.00	7.69
SS39	82.10	28.40	2.89	943.10	8.43
SS79	83.30	29.80	2.80	1026.40	9.17
SS29	83.50	29.20	2.86	1109.90	9.92
SS81	84.40	27.60	3.06	1194.30	10.67
SS15	84.70	30.20	2.80	1279.00	11.43
SS75	85.70	28.60	3.00	1364.70	12.20
SS49	85.90	30.20	2.84	1450.60	12.96
SS60	86.20	31.40	2.75	1536.80	13.73
SS31	86.30	30.80	2.80	1623.10	14.51
SS14	86.30	29.20	2.96	1709.40	15.28
SS94	86.60	29.80	2.91	1796.00	16.05
SS2	88.90	28.80	3.09	1884.90	16.84
SS11	89.40	32.20	2.78	1974.30	17.64
SS77	89.90	29.80	3.02	2064.20	18.45
SS76	91.10	30.40	3.00	2155.30	19.26
SS3	91.80	32.80	2.80	2247.10	20.08
SS43	92.60	30.00	3.09	2339.70	20.91
SS83	92.80	30.40	3.05	2432.50	21.74
SS66	93.50	33.60	2.78	2526.00	22.57
SS90	93.60	30.40	3.08	2619.60	23.41
SS91	94.20	33.20	2.84	2713.80	24.25
SS82	95.40	30.60	3.12	2809.20	25.11
SS35	95.60	34.60	2.76	2904.80	25.96
SS7	95.70	30.40	3.15	3000.50	26.81

Table 2.2 continued: Stone Characteristics for Stone Sample Set Two

Stone	Mass (g)	Average Volume (cm3)	Density (g/cm3)	Cumulative Mass	% Finer by mass
SS64	96.50	30.00	3.22	3097.00	27.68
SS44	96.70	33.60	2.88	3193.70	28.54
SS10	98.10	30.60	3.21	3291.80	29.42
SS8	98.50	33.80	2.91	3390.30	30.30
SS72	99.40	33.20	2.99	3489.70	31.19
SS95	100.50	32.00	3.14	3590.20	32.08
SS41	102.50	38.40	2.67	3692.70	33.00
SS40	103.50	34.40	3.01	3796.20	33.93
SS16	104.60	33.60	3.11	3900.80	34.86
SS74	105.60	36.60	2.89	4006.40	35.80
SS58	106.50	33.80	3.15	4112.90	36.76
SS13	106.70	34.40	3.10	4219.60	37.71
SS50	109.00	36.60	2.98	4328.60	38.68
SS4	110.00	39.80	2.76	4438.60	39.67
SS51	111.10	40.00	2.78	4549.70	40.66
SS68	111.20	36.60	3.04	4660.90	41.65
SS1	111.20	33.40	3.33	4772.10	42.65
SS57	112.50	39.80	2.83	4884.60	43.65
SS59	113.20	40.40	2.80	4997.80	44.66
SS70	113.90	38.80	2.94	5111.70	45.68
SS36	114.00	39.80	2.86	5225.70	46.70
SS93	116.90	41.80	2.80	5342.60	47.75
SS52	117.00	42.40	2.76	5459.60	48.79
SS87	117.60	39.20	3.00	5577.20	49.84
SS86	120.10	40.20	2.99	5697.30	50.92
SS100	121.10	40.00	3.03	5818.40	52.00
SS45	122.40	40.40	3.03	5940.80	53.09
SS33	124.10	44.60	2.78	6064.90	54.20
SS32	124.60	42.60	2.92	6189.50	55.31
SS56	128.70	42.20	3.05	6318.20	56.46
SS61	128.90	40.00	3.22	6447.10	57.62
S47	129.80	48.40	2.68	6576.90	58.78
SS25	130.50	48.80	2.67	6707.40	59.94
SS37	130.50	49.40	2.64	6837.90	61.11
SS6	130.90	48.40	2.70	6968.80	62.28
SS84	131.20	47.00	2.79	7100.00	63.45

Table 2.2 continued: Stone Characteristics for Stone Sample Set Two

Stone	Mass (g)	Average Volume (cm3)	Density (g/cm3)	Cumulative Mass	% Finer by mass
SS63	132.00	42.20	3.13	7232.00	64.63
SS18	133.40	42.80	3.12	7365.40	65.82
SS19	133.40	49.60	2.69	7498.80	67.01
SS34	133.50	44.80	2.98	7632.30	68.21
SS96	134.80	46.80	2.88	7767.10	69.41
SS67	135.00	40.60	3.33	7902.10	70.62
SS98	137.70	46.60	2.95	8039.80	71.85
SS99	138.80	46.80	2.97	8178.60	73.09
SS89	139.10	47.20	2.95	8317.70	74.33
SS92	141.60	45.40	3.12	8459.30	75.60
SS48	141.80	50.40	2.81	8601.10	76.87
SS12	142.10	48.40	2.94	8743.20	78.14
SS62	144.30	47.60	3.03	8887.50	79.43
SS46	145.40	48.60	2.99	9032.90	80.72
SS42	145.70	49.40	2.95	9178.60	82.03
SS22	145.80	49.80	2.93	9324.40	83.33
SS27	146.20	45.60	3.21	9470.60	84.64
SS73	148.20	50.00	2.96	9618.80	85.96
SS17	148.70	49.80	2.99	9767.50	87.29
SS9	150.70	53.40	2.82	9918.20	88.64
SS55	152.40	50.60	3.01	10070.60	90.00
SS28	155.80	51.80	3.01	10226.40	91.39
SS20	156.20	52.40	2.98	10382.60	92.79
SS23	157.20	52.40	3.00	10539.80	94.19
SS69	159.70	52.60	3.04	10699.50	95.62
SS38	161.20	51.60	3.12	10860.70	97.06
SS24	164.10	61.60	2.66	11024.80	98.53
SS5	165.00	60.00	2.75	11189.80	100.00
Total	11189.8	3832	293.0971		
Average	111.90	38.32	2.93		

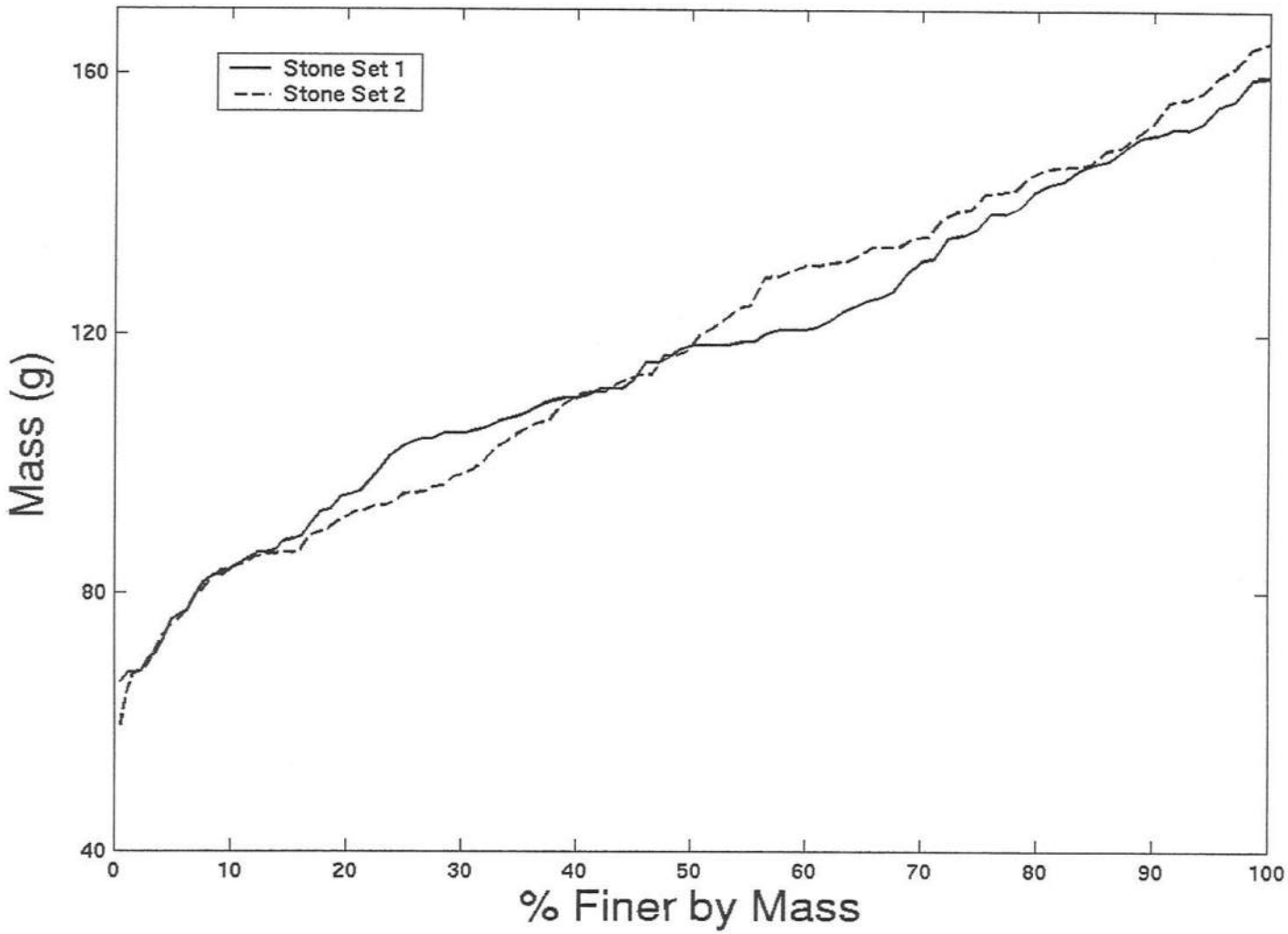

Figure 2.3: % Finer by Mass for Stone Sets One and Two

2.2.3 FREE SURFACE AND VELOCITY MEASUREMENTS

Wave gauges 1 – 3 were located immediately outside the surf zone and used to separate the incident and reflected waves using linear wave theory (Kobayashi et al. 1990). The gauge locations are indicated using the cross-shore coordinate, x, which is taken to be positive onshore, with $x = 0$ at gauge 1. The still water depth at each location was also measured when the water depth, d_c, on top of the structure = 0 cm. These values along with their cross-shore coordinate are show in Table 2.3.

Table 2.3: Still Water Depth at Gauge Locations

Wave Gauge Number	**1**	**2**	**3**	**4**	**5**	**6**	**7**	**8**
Cross-Shore Location x = (m)	0	0.31	1.31	3.21	5.11	6.21	7.26	9.31
Still Water Depth (m)	0.31 + d_c	0.30 + d_c	0.27 + d_c	0.22 + d_c	0.16 + d_c	d_c	0.10 + d_c	0.13 + d_c

The calibration data for wave gauges 1-8 generally followed a linear line, as illustrated for gauge 1, as an example, in Figure 2.4. The best fit slope to all the data points was obtained for each of these gauges. This slope is shown in Figure 2.4 as the solid line. The points obtained in the calibration are represented as the dots. Calibration for gauges 1 – 8 was performed frequently to ensure the reliability of the calibration curves.

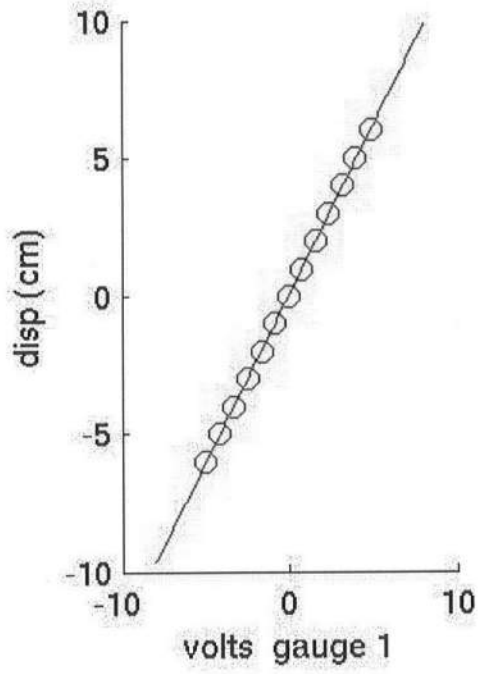

Figure 2.4: Calibration Curve for Wave Gauge 1

The measured values of the spectral peak period, T_p, and $H_{rms} = \sqrt{8}\,\sigma_\eta$ at wave gauge 1 as well as the incident root-mean-square wave height, $(H_{rms})_i$ and the average reflection coefficient, $R = (H_{rms})_r / (H_{rms})_i$, with $(H_{rms})_r$ = reflected root-mean-square wave height, are listed in Table 2.4. The values listed in Table 2.4 and subsequent tables show the measured values in repeated runs. The repeated runs were used to check the reliability of the measurements in the region of intense wave breaking in shallow water. All the measured values are plotted in the subsequent figures to show the degree of

scatter of the measured values except for one value from wave gauge 5 and ADV 1 and two values from ADV 2 in Figure 2.2. In Table 2.4 $R = 0.16 - 0.20$ but the difference between H_{rms} and $(H_{rms})_i$ is less than approximately 3%. It should be noted that wave reflection is neglected in the proposed time-averaged model.

Table 2.4: Measured Wave Characteristics at Wave Gauge 1

		Total		Incident		Reflected	
Test	**Run**	**Hrms (cm)**	**Tp (sec)**	**Hrms (cm)**	**Tp (sec)**	**Hrms (cm)**	**R**
R4	**1**	10.27	2.32	9.88	2.32	1.76	0.178
	2	10.24	2.32	9.00	2.32	1.79	0.181
	3	10.30	2.32	10.00	2.32	1.74	0.174
	4	10.33	2.32	9.99	2.32	1.78	0.178
	5	10.26	2.32	9.91	2.32	1.74	0.175
	Avg.	**10.28**	**2.32**	**9.94**	**2.32**	**1.76**	**1.77**
R6	**1**	10.22	2.32	10.06	2.32	1.72	0.171
	2	10.15	2.32	9.89	2.54	1.72	0.174
	3	10.31	2.32	10.05	2.32	1.75	0.174
	Avg.	**10.23**	**2.32**	**10.00**	**2.39**	**1.73**	**0.173**
R8	**1**	10.71	2.31	10.58	2.31	1.75	0.165
	2	10.45	2.32	10.39	2.32	1.69	0.163
	Avg.	**10.58**	**2.32**	**10.49**	**2.32**	**1.72**	**0.164**
R10	**1**	10.70	2.32	10.41	2.32	2.12	0.204
	2	10.92	2.32	10.64	2.32	2.10	0.198
	Avg.	**10.81**	**2.32**	**10.53**	**2.32**	**2.11**	**0.201**

Table 2.5 lists the free surface elevation, $\bar{\eta}$, above SWL measured at wave gauges 1 – 8, where overbar denotes time-averaging. Wave setdown, $\left(-\bar{\eta}\right)$, was approximately 0.5 cm at $x = 0$ and wave setup, $\bar{\eta}$, at wave gauges 7 and 8 increased with the decrease of d_c. In the following tables, NR implies "not reliable" and represents data that was

collected but was not consistent with the other repeated runs. Figure 2.5 shows the plot of the data measured in order to see the trends more easliy. Table 2.6 lists the standard deviation, σ_η, of the free surface elevation, η, above SWL measured at wave gauges 1 – 8. The seaward toe of the breakwater was located at x = 5.11 m where the still water depth was (d_c + 16.2) cm. Some of the large incident waves broke on the 1/35 slope. Incident waves broke intensely on the 1/2.28 slope of the breakwater. These breaker patterns are consistent with the measured cross-shore variation of σ_η which decreased rapidly from wave gauges 5 to wave gauge 6 located in the middle of the crest of the breakwater. The transmitted values of σ_η at wave gauges 7 and 8 increased with the increase of the depth d_c as expected from available formulas of wave transmission (van der Meer and Daemen 1994). Figure 2.6 shows the plot of the data measured.

Table 2.7 lists the mean, $\bar{u}$, and standard deviation, σ_u, of the cross-shore horizontal velocity, u, measured by ADV 1 – 3. ADV 1 measured u at z_m = 7 cm in the still water depth of (d_c + 16.5) cm where z_m is the vertical distance above the local bottom. The still water depth is d_c and (d_c + 2.9) cm at ADV 2 and 3, respectively, which measured u at z_m = 3.5 cm for tests R6, R8 and R10. For test R4, ADV 2 and 3 measured u at z_m = 1 and 2 cm, respectively, so that these velocimeters were not exposed to air during test R4. In short, ADV 1 – 3 measured u in the region near the local bottom. The mean current, $\bar{u}$, was negative and flowed in the seaward direction. The standard deviation σ_u of the fluctuating velocity including the wave and turbulent components increased with the increase of d_c at ADV 2 and 3 but did not change much at ADV 1. The vertical and cross-flume velocities measured by ADV 1 – 3 appeared to be

dominated by the turbulent velocities and were much smaller than the cross-shore velocity, u, which was dominated by the wave component. Figures 2.7 and 2.8 show plots of the mean and standard deviation of the velocity data.

Table 2.5: Measured Mean Free Surface Elevation , $\bar{\eta}$ (cm)

Test	Run	x (m)=0	0.308	1.308	3.208	5.108	6.208	7.258	9.308
R4	1	-0.42	-0.39	-0.39	-0.17	-0.51	1.149	1.45	1.45
	2	-0.58	-0.51	-0.55	-0.64	-0.47	1.10	1.41	1.39
	3	-0.57	-0.53	-0.51	-0.64	-0.23	1.02	1.34	1.33
	4	-0.52	-0.49	-0.50	-0.73	-0.45	1.04	1.35	1.33
	5	-0.42	-0.38	-0.37	-0.45	NR	1.10	1.42	1.39
	Avg.	**-0.50**	**-0.46**	**-0.46**	**-0.53**	**-0.42**	**1.08**	**1.39**	**1.38**
R6	1	-0.58	-0.61	-0.63	-0.67	NR	0.60	0.97	0.96
	2	-0.57	-0.60	-0.51	-0.74	-0.53	0.54	0.84	0.83
	3	-0.57	-0.59	-0.54	-0.57	-0.54	0.58	0.95	0.94
	Avg.	**-0.57**	**-0.60**	**-0.56**	**-0.66**	**-0.54**	**0.57**	**0.92**	**0.91**
R8	1	-0.51	-0.50	-0.56	-0.63	-0.31	0.28	0.69	0.72
	2	-0.52	-0.53	-0.43	-0.58	-0.06	0.41	0.69	0.73
	Avg.	**-0.52**	**-0.52**	**-0.50**	**-0.61**	**-0.19**	**0.35**	**0.69**	**0.73**
R10	1	-0.41	-0.44	-0.16	-0.51	-0.38	0.13	0.60	0.57
	2	-0.42	-0.48	-0.19	-0.48	-0.56	0.13	0.53	0.55
	Avg.	**-0.42**	**-0.46**	**-0.18**	**-0.50**	**-0.47**	**0.13**	**0.57**	**0.56**

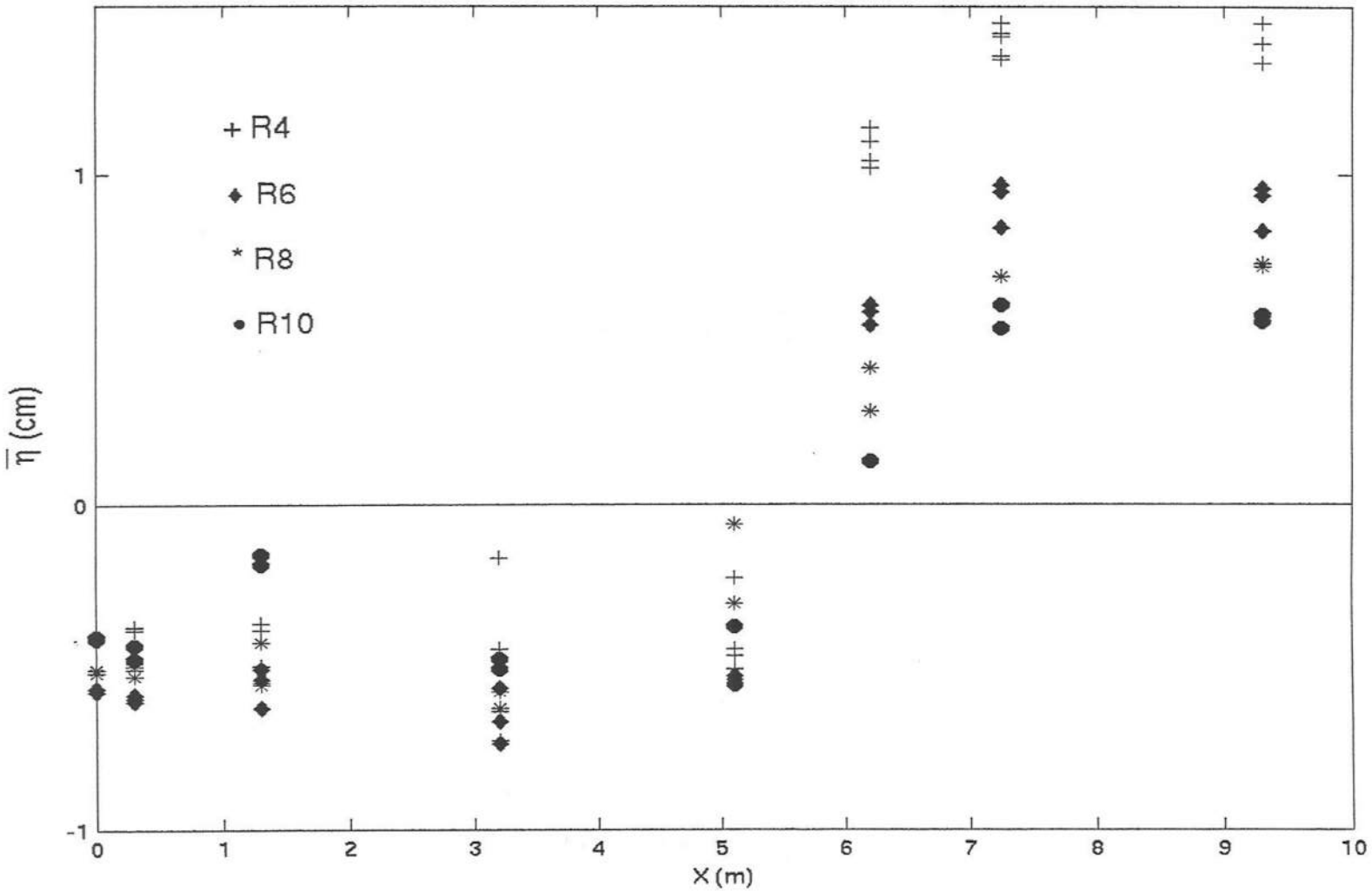

Figure 2.5: Measured Cross-Shore Variations of Mean Free Surface Elevation, $\overline{\eta}$ (cm)

Table 2.6: Standard Deviation of the Free Surface Elevation, σ_η (cm)

Test	Run	x (m)=0	0.308	1.308	3.208	5.108	6.208	7.258	9.308
R4	1	3.63	3.59	3.60	3.26	3.28	1.76	1.21	1.23
	2	3.62	3.61	3.60	3.28	3.26	1.69	1.17	1.17
	3	3.64	3.66	3.60	3.32	3.24	1.76	1.21	1.21
	4	3.65	3.66	3.60	3.03	3.24	1.75	1.21	1.21
	5	3.63	3.61	3.62	3.32	NR	1.76	1.21	1.23
	Avg.	**3.63**	**3.63**	**3.61**	**3.24**	**3.26**	**1.74**	**1.20**	**1.21**
R6	1	3.61	3.58	3.71	3.36	3.35	1.96	1.35	1.36
	2	3.59	3.55	3.56	3.27	3.38	1.97	1.38	1.37
	3	3.65	3.62	3.64	3.12	3.76	1.94	1.35	1.33
	Avg.	**3.62**	**3.58**	**3.64**	**3.25**	**3.50**	**1.96**	**1.36**	**1.35**
R8	1	3.80	3.74	3.76	3.50	3.53	2.21	1.6	1.61
	2	3.69	3.68	3.79	3.51	3.57	2.25	1.62	1.61
	Avg.	**3.75**	**3.71**	**3.78**	**3.51**	**3.55**	**2.23**	**1.61**	**1.61**
R10	1	3.78	3.82	3.63	3.70	3.83	2.59	1.92	1.90
	2	3.86	3.89	3.70	3.73	3.82	2.61	1.91	1.89
	Avg.	**3.82**	**3.86**	**3.86**	**3.72**	**3.83**	**2.60**	**1.92**	**1.90**

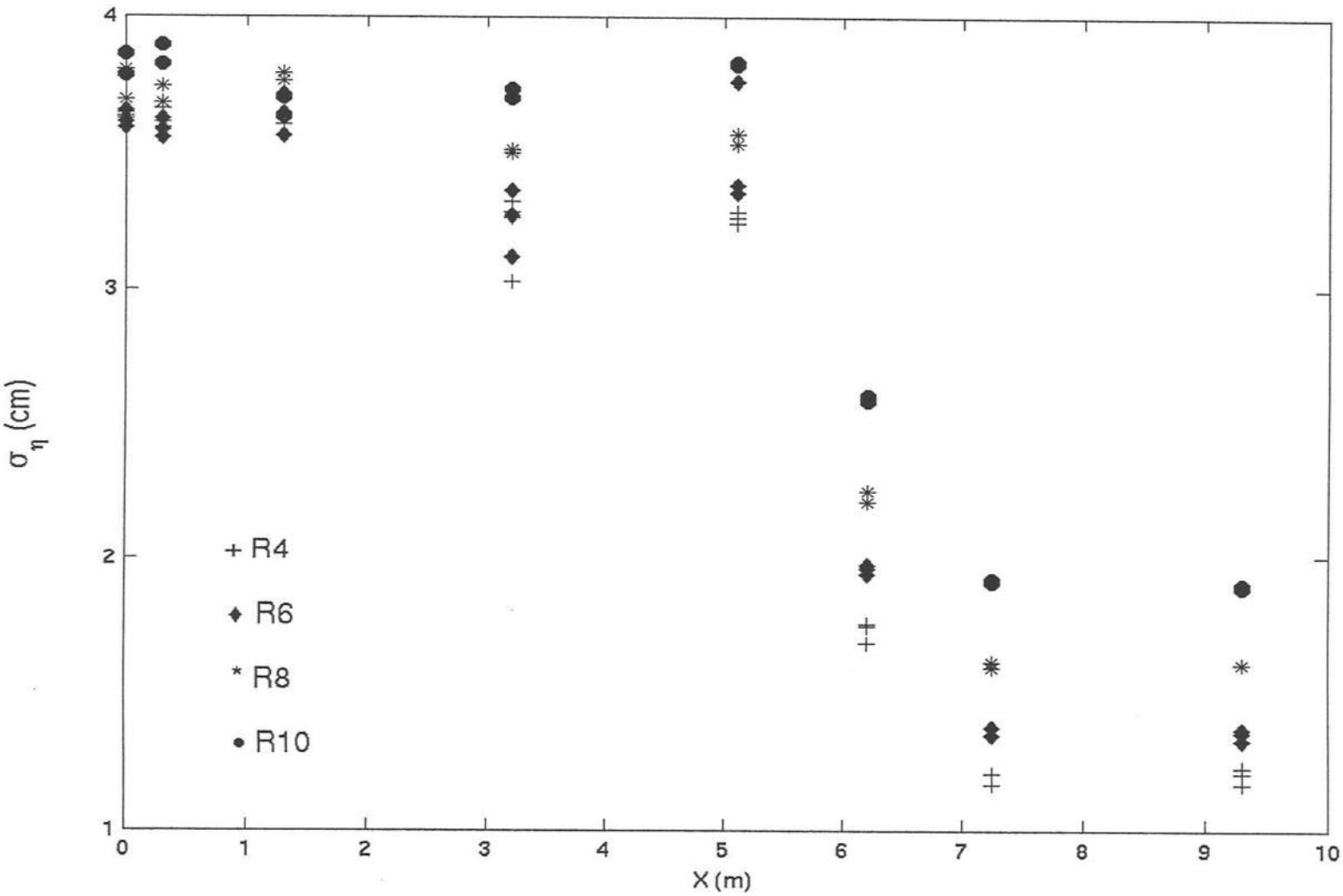

Figure 2.6: Measured Cross-Shore Variations of Standard Deviation of Free Surface Elevation, σ_η

Table 2.7: Mean and Standard Deviation of Horizontal Velocity (cm/s) at x = 5.008, 6.108, and 7.158 m

		Mean			Standard Deviation		
Test	**run**	**x=5.008**	**6.108**	**7.158**	**x=5.008**	**6.108**	**7.158**
R4	**1**	-1.98	-2.55	-2.42	18.71	11.74	11.75
	2	-2.75	-2.52	-2.40	19.64	11.71	13.20
	3	-2.10	**NR**	-2.46	20.11	15.15	11.46
	4	-2.56	-2.42	-2.63	18.83	11.64	11.48
	5	-2.12	-2.44	-1.78	19.03	11.75	11.87
	Avg.	**-2.30**	**-2.48**	**-2.34**	**19.26**	**12.40**	**11.95**
R6	**1**	-2.05	-2.11	-0.44	18.13	20.51	14.91
	2	-2.04	-1.82	-1.52	19.09	**NR**	14.57
	3	-1.78	-4.33	-1.66	18.92	19.12	14.13
	Avg.	**-1.96**	**-2.75**	**-1.21**	**18.71**	**19.82**	**14.54**
R8	**1**	-2.05	-3.75	-1.96	17.60	19.30	14.75
	2	-1.28	-4.36	-3.06	**NR**	23.16	15.47
	Avg.	**-1.67**	**-4.06**	**-2.51**	**17.60**	**21.23**	**15.11**
R10	**1**	-2.09	-2.00	-4.08	18.17	23.11	17.22
	2	-1.65	-3.31	-5.34	18.04	20.68	15.21
	Avg.	**-1.87**	**-2.66**	**-4.71**	**18.11**	**21.90**	**16.22**

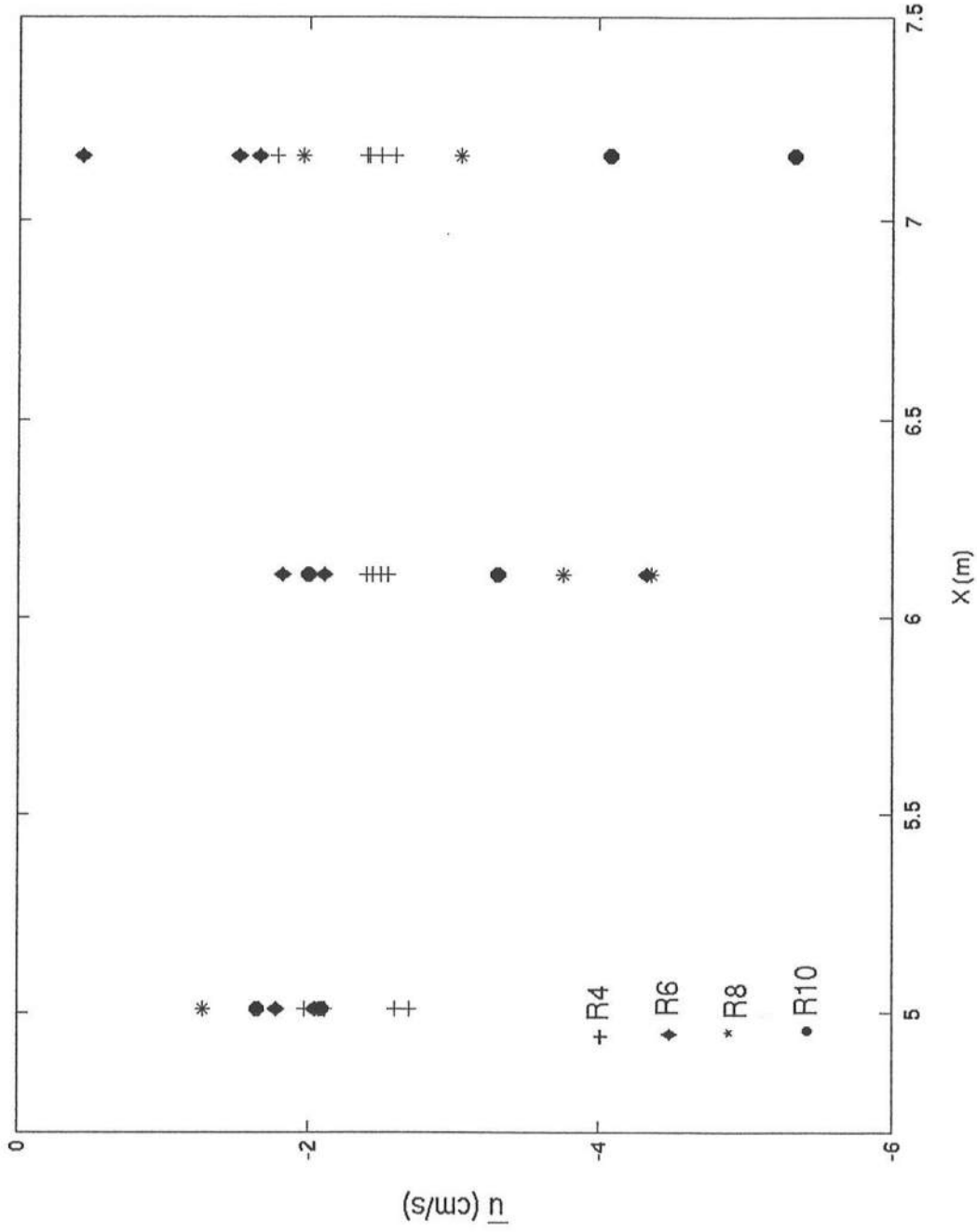

Figure 2.7: Measured Cross-Shore Variations of Mean Horizontal Velocity, $\bar{u}$

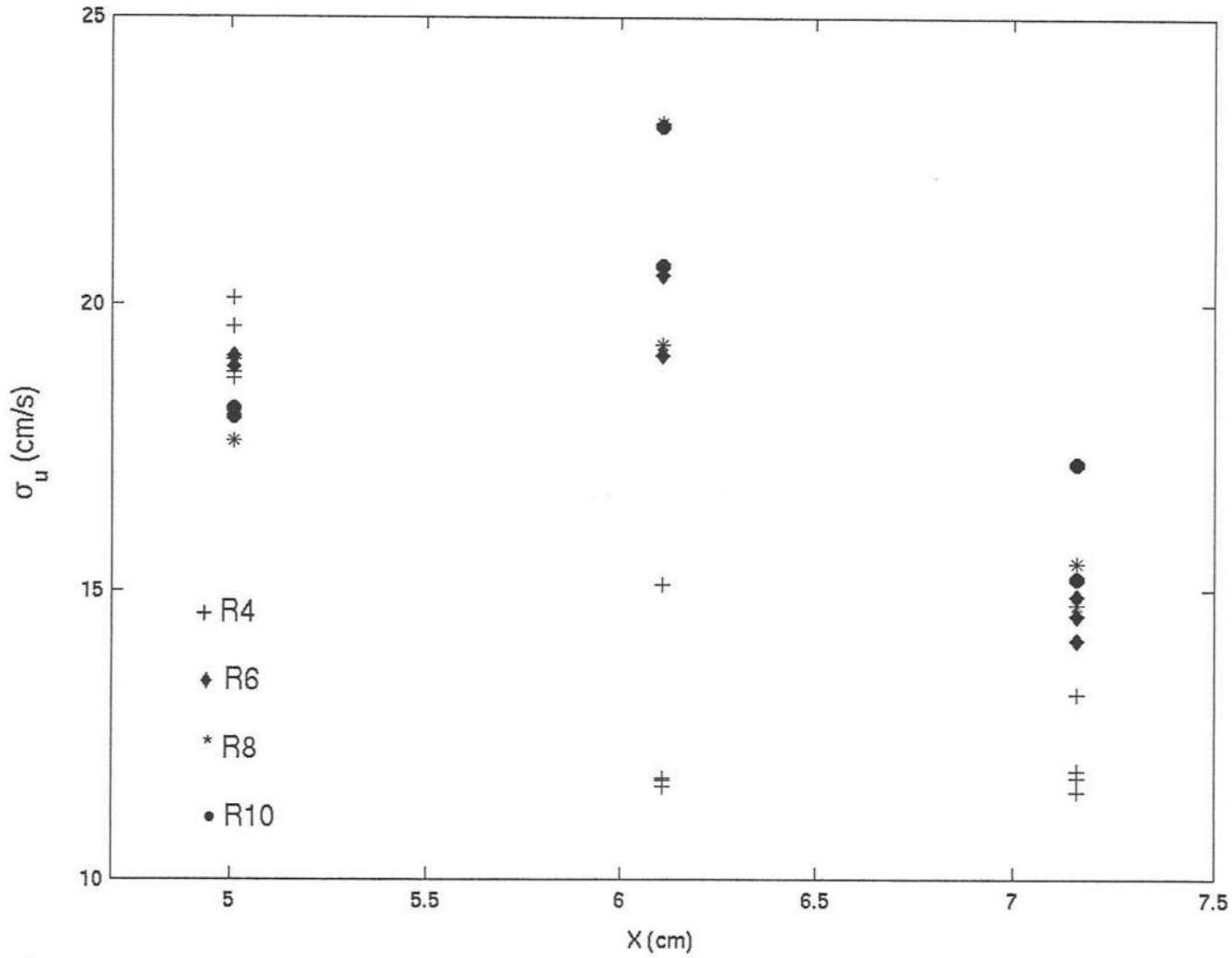

Figure2.8: Measured Cross-Shore Variations of Standard Deviation of Horizontal Velocity, σ_u

2.3 NUMERICAL MODEL

The time-dependent, one-dimensional model in shallow water developed by Kobayashi and Wurjanto (1990) and Wurjanto and Kobayashi (1993) is time-averaged and simplified in the following. The time-averaged cross-shore momentum and energy equations may be expressed as

$$\frac{dS_{xx}}{dx} = -\rho g \bar{h} \frac{d\bar{\eta}}{dx} - \tau_b \tag{2.2}$$

$$\frac{dF}{dx} = -D_B - D_f - D_r \tag{2.3}$$

where S_{xx} = cross-shore radiation stress; ρ = fluid density; g = gravitational acceleration; $\bar{h}$ = mean water depth given by $\bar{h} = \left(\bar{\eta} - z_b\right)$ with z_b = bottom elevation and $z_b < 0$ below SWL; τ_b = bottom shear stress; F = wave energy flux per unit width; and D_B, D_f and D_r = energy dissipation rate per unit horizontal area due to wave breaking, bottom friction, and porous flow resistance, respectively. Equation (2.2) neglects the momentum flux into and out of the porous structure. Equation (2.2) assumes that the energy flux into the porous structure equals the energy dissipation rate, D_r, inside the porous structure.

Neglecting reflected and evanescent waves (Méndez et al. 2001) as well as nonlinear effects (Svendsen et al. 2003), linear wave theory for onshore progressive waves is used to estimate S_{xx} and F (Battjes and Stive 1985)

$$S_{xx} = \rho g \sigma_\eta^2 \left(2n - 0.5\right) \quad ; \quad F = \rho g n C_p \sigma_\eta^2 \tag{2.4}$$

with

$$n=\frac{1}{2}\left[1+\frac{2k_p\bar{h}}{\sinh\left(2k_p\bar{h}\right)}\right] \quad ; \quad C_p=\frac{gT_p}{2\pi}\tanh\left(k_p\bar{h}\right) \tag{2.5}$$

where n = ratio between the group velocity and the phase velocity, C_p; and k_p = linear wave number in the mean water depth, $\bar{h}$, corresponding to the spectral peak period, T_p, which is assumed to be constant. In the experiment, the frequency spectra for η changed due to the generation of lower and higher harmonics especially after wave breaking on the structure. Nevertheless, $n = 1$ and $C_p=\sqrt{g\bar{h}}$ in shallow water for any representative wave period. The cross-shore variations of $\bar{\eta}$ and $H_{rms}=\sqrt{8}\,\sigma_\eta$ on impermeable beaches are normally predicted using Equations (2.2) – (2.5) with $\tau_b = 0$, $D_f = 0$ and $D_r = 0$. These neglected terms may be important for porous structures and beaches consisting of coarse materials.

The time-averaged bottom shear stress, τ_b, and the corresponding dissipation rate , D_f, are expressed as (Kobayashi and Johnson 1998)

$$\tau_b=\frac{1}{2}\rho f_b\overline{|u|u} \quad ; \quad D_f=\frac{1}{2}\rho f_b\overline{|u|u^2} \tag{2.6}$$

where the overbar denotes time averaging and f_b is the bottom friction factor. It is assumed in the following computation that $f_b = 0$ on the smooth slope and $f_b = 0.01$ –

0.05 on the stone structure. To express τ_b and D_f in terms of $\bar{u}$ and σ_u, the equivalency of the time and probabilistic averaging as well as the Gaussian distribution of u are assumed (Kobayashi et al. 1998). These assumptions yield

$$\tau_b = \frac{1}{2}\rho f_b \sigma_u^2 G_2(u_*) \quad ; \quad D_f = \frac{1}{2}\rho f_b \sigma_u^3 G_3(u_*) \quad ; \quad u_* = \frac{\bar{u}}{\sigma_u} \tag{2.7}$$

with

$$G_2(u_*) = \frac{1}{\sqrt{2\pi}} \int_{-\infty}^{\infty} |y+u_*|(y+u_*)\exp\left(-\frac{y^2}{2}\right)dy \tag{2.8}$$

$$G_3(u_*) = \frac{1}{\sqrt{2\pi}} \int_{-\infty}^{\infty} |y+u_*|^3 \exp\left(-\frac{y^2}{2}\right)dy \tag{2.9}$$

Equations (2.8) and (2.9) can be integrated analytically

$$G_2(r) = \left(1+r^2\right)\mathrm{erf}\left(\frac{r}{\sqrt{2}}\right) + \sqrt{\frac{2}{\pi}}\, r \exp\left(-\frac{r^2}{2}\right) \tag{2.10}$$

$$G_3(r) = \left(3r+r^3\right)\mathrm{erf}\left(\frac{r}{\sqrt{2}}\right) + \sqrt{\frac{2}{\pi}}\left(r^2+2\right)\exp\left(-\frac{r^2}{2}\right) \tag{2.11}$$

where erf = error function and r = arbitrary variable with $r = u_*$ in Equation (2.7). The functions G_2 and G_3 for the range $|r| < 1$ can be approximated as $G_2 = 1.64\ r$ and $G_3 = (1.6 + 2.6\ r^2)$. For the actual computation, use is made of Equations (2.10) and (2.11) because the error function is easy to calculate. The analytical functions $G_2(r)$ and $G_3(r)$ are plotted as a function of the arbitrary variable r in Figure 2.9.

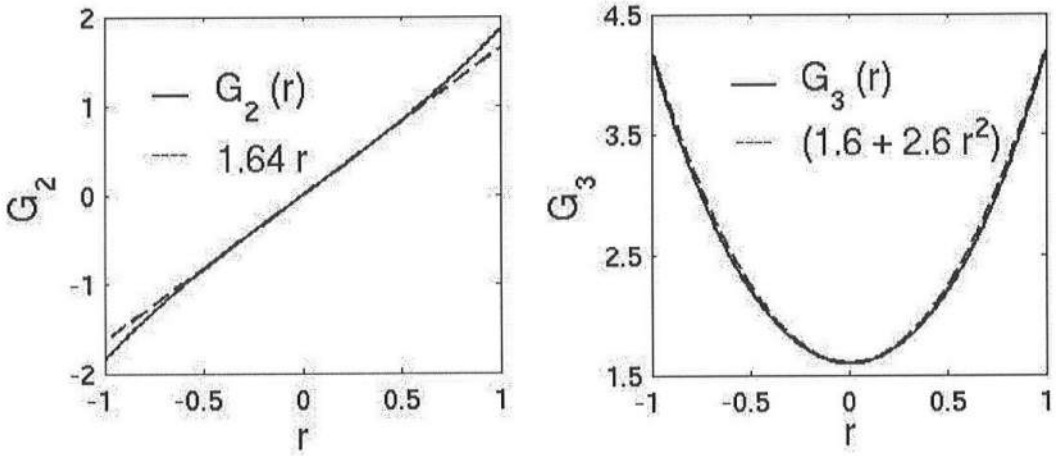

Figure 2.9: Functions G_2 and G_3 and Fitted Equations

The standard deviation, σ_u, in Equation (2.7) is estimated using the relationship between σ_u and σ_η based on linear shallow-water wave theory (Kobayashi et al. 1998)

$$\sigma_u = \sqrt{g\bar{h}}\,\sigma_* \quad ; \quad \sigma_* = \sigma_\eta / \bar{h} \tag{2.12}$$

where u does not vary vertically because of the assumption of shallow water. The offshore (return) current, $\bar{u}$, in Equation (2.7) is estimated using the time-averaged, vertically-integrated continuity equation along with the condition of no water flux into the impermeable 1/35 slope

$$\sigma_u \sigma_\eta + \bar{u}\bar{h} + \bar{v} h_p = 0 \tag{2.13}$$

where $\sigma_u \sigma_\eta$ is the onshore flux due to linear shallow-water waves (Kobayashi et al. 1998), $\bar{u}\bar{h}$ is the offshore flux due to the return current, $\bar{u}$, and $\bar{v} h_p$ is the water flux inside the porous structure with its local vertical height, h_p, due to the time-averaged horizontal discharge velocity, $\bar{v}$, which is assumed to be invariant vertically. Substitution of Equation (2.12) into Equation (2.13) yields

$$\bar{u} = -\left(\sqrt{g\bar{h}}\,\sigma_*^2 + \bar{v} h_p / \bar{h}\right) \tag{2.14}$$

The vertical height, h_p, is obtained using $h_p = (z_b - z_p)$ where $z_b(x)$ and $z_p(x)$ are the bottom profile and the impermeable slope specified as input to the numerical model where $h_p = 0$ in the region of no porous structure in Figure. 2.1.

Neglecting the inertia terms in the horizontal momentum equation for the flow inside the porous structure (Kobayashi and Wurjanto 1990), the local force balance between the horizontal pressure gradient and flow resistance is assumed

$$-g\frac{\partial \eta}{\partial x} = \alpha v + \beta |v| v \tag{2.15}$$

where the pressure is assumed to be hydrostatic below the instantaneous free surface elevation, η, in shallow water. The coefficients α and β express the laminar and turbulent flow resistance. Van Gent (1995) conducted oscillating water tunnel experiments and proposed the following formulas

$$\alpha = \alpha_o \frac{\left(1-n_p\right)^2}{n_p^2} \frac{\nu}{D_{n50}^2} \quad ; \quad \beta = \beta_1 + \frac{\beta_2}{\sigma_v} \tag{2.16}$$

with

$$\beta_1 = \frac{\beta_o \left(1-n_p\right)}{n_p^3 D_{n50}} \quad ; \quad \beta_2 = \frac{7.5\beta_o \left(1-n_p\right)}{\sqrt{2}\, n_p^2 T_p} \tag{2.17}$$

where α_o = empirical parameter calibrated as α_o = 1,000; n_p = porosity of the stone; ν = kinematic viscosity of the fluid; D_{n50} = nominal stone diameter; β_o = empirical parameter calibrated as β_o = 1.1; T_p = spectral peak period used here to represent the monochromatic

wave period in his experiments; and σ_v = standard deviation of the horizontal discharge velocity, v. The velocity amplitude of sinusoidal oscillation in his experiments is taken as $\sqrt{2}\,\sigma_v$ to yield the same standard deviation. In the following computation, use is made of $\alpha_o = 1{,}000$ and $\beta_o = 1 - 5$.

Two equations for $\bar{v}$ and σ_v will be obtained from Equation (2.15). The energy dissipation rate, D_r, due to the porous flow resistance in Equation (2.3) is expressed as (Wurjanto and Kobayashi 1993)

$$D_r = \rho h_p \left(\alpha \overline{v^2} + \beta \overline{|v| v^2} \right) \tag{2.18}$$

Assuming the equivalency of the time and probabilistic averaging and the Gaussian distribution of v, Equation (2.18) is expressed in terms of the mean $\bar{v}$ and standard deviation σ_v

$$D_r = \rho h_p \left[\alpha \sigma_v^2 \left(1 + v_*^2 \right) + \beta \sigma_v^3 G_3 \left(v_* \right) \right] \quad ; \quad v_* = \frac{\bar{v}}{\sigma_v} \tag{2.19}$$

where the function G_3 is given by Equation (2.11). Similarly, time-averaging Equation (2.15) yields

$$-g \frac{d\bar{\eta}}{dx} = \alpha \bar{v} + \beta \sigma_v^2 \, G_2 \left(v_* \right) \tag{2.20}$$

where the function G_2 is given by Equation (2.10). To obtain an explicit equation for $\bar{v}$, Equation (2.20) is approximated as

$$-g\frac{d\bar{\eta}}{dx} = \bar{v}\left[\alpha + 1.64\left(\beta_1\sigma_v + \beta_2\right)\right] \tag{2.21}$$

where use is made of Equation (2.16) and $G_2(v_*) = 1.64\, v_*$ for $|v_*| < 1$.

An equation for σ_v cannot be derived from Equation (2.15) without additional approximations. To overcome this closure problem, Equation (2.15) is linearized as

$$-g\frac{\partial\eta}{\partial x} = \left(\alpha + \beta C_v\sigma_v\right)v \tag{2.22}$$

The dimensionless coefficient C_v is chosen to yield the same dissipation rate, D_r, given by Equation (2.18)

$$\left(\alpha + \beta C_v\sigma_v\right)\overline{v^2} = \alpha\overline{v^2} + \beta\overline{|v|v^2} \tag{2.23}$$

which yields $C_v = G_3\left(v_*\right)/\left(1+v_*^2\right)$ with $v_* = \bar{v}/\sigma_v$. For the typical range $|v_*| < 0.5$, C_v = 1.6 – 2.2 and use is made of C_v = 1.9 to simplify the computation of σ_v as explained in the following and as seen in Figure 2.10. The following equation for $\sigma_v^2 = \overline{\left(v-\bar{v}\right)^2}$ can be derived from Equation (2.22)

$$\left(\alpha+\beta C_v\sigma_v\right)^2\sigma_v^2=g^2\overline{\left[\frac{\partial\left(\eta-\bar{\eta}\right)}{\partial x}\right]^2} \tag{2.24}$$

The monochromatic approximation of $\left(\eta-\bar{\eta}\right)=\sqrt{2}\,\sigma_\eta\cos\left(\omega_p t-k_p x\right)$ with $\omega_p=\left(2\pi/T_p\right)$ in Equation (2.24) yields

$$\alpha\sigma_v+\beta C_v\sigma_v^2=g\,k_p\,\bar{h}\,\sigma_* \quad ; \quad \sigma_*=\frac{\sigma_\eta}{\bar{h}} \tag{2.25}$$

The quadratic equation (2.25) with $\beta=\left(\beta_1+\beta_2/\sigma_v\right)$ can be solved analytically to obtain σ_v for known $k_p\bar{h}\sigma_*$ where the use of σ_* in this equation will be explained later. After σ_v is obtained, Equation (2.21) is used to calculate $\bar{v}$ for known $d\bar{\eta}/dx$.

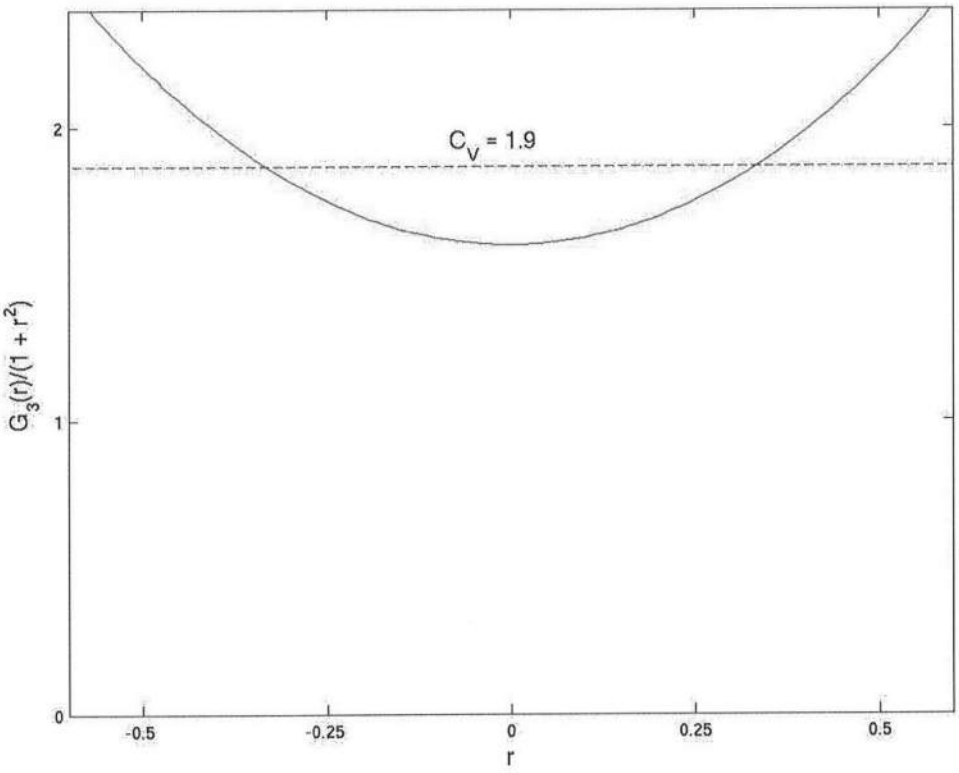

Figure 2.10: Dimensionless Coefficient, C_v

Finally, the energy dissipation rate, D_B, due to wave breaking in Equation (2.3) is estimated using the formula by Battjes and Stive (1985)

$$D_B = \frac{\rho g a Q H_B^2}{4T_p} \quad ; \quad \frac{Q-1}{\ln Q} = \left(\frac{H_{rms}}{H_m}\right) \quad ; \quad H_m = \frac{0.88}{k_p}\tanh\left(\frac{\gamma k_p \bar{h}}{0.88}\right) \qquad (2.26)$$

where a = empirical coefficient suggested as $a = 1$; Q = fraction of breaking waves with $Q = 0$ for no wave breaking and $Q = 1$ when all waves break; H_B = wave height used to

estimate D_B with $H_B = H_m$ in their formula; H_m = local depth-limited wave height; and γ = breaker ratio parameter with $H_m = \gamma \bar{h}$ in shallow water. Equation (2.26) is widely used to predict D_B in surf zones on beaches in the absence of structures. However, Battjes and Janssen (1978) indicated that D_B given by Equation (2.26) would underestimate the actual energy dissipation rate and produce $H_{rms} > H_m$ in very shallow water, although the requirement of $0 \le Q \le 1$ requires $H_{rms} \le H_m$.

The modifications of Equation (2.26) made here are discussed in the following. The choice of a = 1 was based on the assumption of the energy dissipation of a bore distributed uniformly over one wavelength. This assumption does not appear to be reasonably physically in the region where the energy dissipation is more concentrated locally. The coefficient a is hence taken as the ratio of the wavelength estimated as $T_p\sqrt{g\bar{h}}$ to the horizontal length scale $\left(b\bar{h}/S_b\right)$ with b = empirical factor, imposed by the small depth $\bar{h}$ and the local bottom slope, $S_b = dz_b / dx$

$$a = \frac{T_p S_b \sqrt{g}}{b\sqrt{\bar{h}}} \ge 1 \tag{2.27}$$

where $a \ge 1$ is imposed so that $a = 1$ in the region of large $\bar{h}$ and small S_b. The bottom slope, S_b, is positive in the region where the bottom elevation, z_b, increases landward. For the submerged breakwater shown in Figure 2.1, S_b = 0.44 on the seaward slope and

$S_b \leq 0$ on the crest and landward slope. Equation (2.27) increases D_B only on the seaward slope where intense wave breaking occurred. The slope adjustment factor, b, in Equation (2.27) is calibrated in the range $b = 2 - 3$ on the basis of the following approximate analysis. It may be noted that D_B can also be increased by increasing γ because $H_m = \gamma \bar{h}$ in shallow water where γ was observed to increase with the beach slope (Raubenheimer et al. 1996). The value of γ is held constant here and calibrated in the range $\gamma = 0.6 - 0.7$ to obtain good agreement seaward of the structure.

Equation (2.2) with $\tau_b = 0$ and Equation (2.3) with $D_f = 0$ and $D_r = 0$ along with Equation (2.4) with $n = 1$ and $C_p = \sqrt{g\bar{h}}$ yield

$$\left[1 - \frac{3}{4}\left(\frac{\sigma_\eta}{\bar{h}}\right)^2\right]\frac{d\sigma_\eta}{dx} ; \frac{\sigma_\eta}{4\bar{h}}\left[S_b - \frac{4aQ\bar{h}}{T_p\sqrt{g\bar{h}}}\left(\frac{H_B}{H_{rms}}\right)^2\right] \tag{2.28}$$

where use is made of Equation (2.26) and $H_{rms} = \sqrt{8}\,\sigma_\eta$. Equation (2.28) with $\sigma_\eta < \bar{h}$ indicates that σ_η increases landward on the positive slope, S_b, due to wave shoaling. This increase has been found to be too large on the slope S_b =0.44 for the case of $a = 1$. Substitution of Equation (2.27) into Equation (2.28) yields

$$\left[1 - \frac{3}{4}\left(\frac{\sigma_\eta}{\bar{h}}\right)^2\right]\frac{d\sigma_\eta}{dx} ; \frac{\sigma_\eta S_b}{4\bar{h}}\left[1 - \frac{4Q}{b}\left(\frac{H_B}{H_{rms}}\right)^2\right] \quad \text{for} \quad a > 1 \tag{2.29}$$

In the region of intense wave breaking on the slope S_b = 0.44, $H_{rms} > H_m$ and D_B in Equation (2.26) is estimated using $Q = 1$ and $H_B = H_{rms}$ instead of $H_B = H_m$. Then, σ_η decreases landward if $b < 4$ in Equation (2.29). The range of $b = 1 - 4$ was considered initially but the computed results for $b = 2 - 3$ are presented subsequently.

On the other hand, on the crest and landward slope where $S_b \leq 0$, Q in Equation (2.26) is estimated using $H_m = H_e$ with H_e being the wave height H_{rms} at the seaward edge of the crest to ensure $Q < 1$ in the region of $S_b \leq 0$ where some of the waves forced to break on the seaward slope ceased breaking. The dissipation rate, D_B, is calculated using $H_B = H_{rms}$ with Q estimated using $H_m = H_e$. In short, H_B in Equation (2.26) is taken as the local height H_{rms} in the region of $Q = 1$ and $S_b \leq 0$ because the empirical formula for H_m in Equation (2.26) is not really applicable in these regions.

In the region of $H_{rms} > H_m$ and $Q = 1$, $\sigma_* = \sigma_\eta / \bar{h}$ in Equations (2.12), (2.14), and (2.25) becomes large and the computed absolute values of σ_u, $\bar{u}$, σ_v and $\bar{v}$ are too large and vary too rapidly because the mean depth, $\bar{h}$, varies rapidly on the seaward slope of the breakwater. To remedy this shortcoming caused by the local use of linear shallow-water wave theory, use is made of $\sigma_* = \left(\sigma_{*_c} \sigma_\eta / \bar{h}\right)^{0.5}$ if $\sigma_* > \sigma_{*_c} = \gamma / \sqrt{8}$ which corresponds to $H_{rms} = \gamma \bar{h}$. This empirical correction reduces the dependency on the mean water depth, $\bar{h}$. For example, $\sigma_u = \left(\sigma_{*_c} g \, \sigma_\eta\right)^{0.5}$ if $\sigma_* > \sigma_{*_c}$.

In summary, the numerical model is based on Equations (2.2) –(2.5), (2.7), (2.12), (2.14), (2.19), (2.21), (2.25) – (2.27) and the adjustments for the submerged structure explained above. Equations (2.2) and (2.3) are solved using the finite different method with constant nodal spacing, Δx, developed by Kobayashi and Johnson (1998) for the case of $D_r = 0$. The bottom elevation, $z_b(x)$, and the impermeable slope, $z_p(x)$, are specified as input. The stone is characterized by its nominal diameter, D_{n50}, and porosity, n_p, whereas the kinematic viscosity of water is $\nu = 0.01$ cm^2/s. The measured values of $T_p, \bar{\eta}$ and H_{rms} are specified at the seaward boundary $x = 0$. In the following, the landward-marching computation is made in the region $0 \le x \le 10$ m in Figure 2.2 using $\Delta x = 1$ cm. The computation time is of the order of one second in comparison to the computation time of one hour for the time-dependent model by Wurjanto and Kobayashi (1993).

2.4 COMPARISON BETWEEN EXPERIMENTS AND NUMERICAL MODEL

The numerical model is compared with tests R4, R6, R8 and R10 whose data are summarized in Tables 2.4 – 2.7. The calibrated empirical parameters are the bottom friction factor, f_b, on the stone structure in Equation (2.7), the turbulent porous flow resistance factor, β_o, in Equation (2.17), the breaker ratio parameter, γ, in Equation (2.26), and the slope adjustment factor, b, in Equation (2.27). It is noted that the agreement with the data was marginal until the breaker adjustments for the coastal structure explained in relation to Equation (2.27) were introduced to represent the breaker pattern on the structure more realistically. First, the computed results using $f_b = 0.01$, $\beta_o = 5$, $\gamma = 0.7$,

and $b = 2$ and 3 are presented for test R6 as an example. Second, the sensitivities to f_b, β_o and γ are shown for test R6. Third, the compared results for tests R4, R8 and R10 are shown.

Figure 2.11 shows the measured and computed cross-shore variations of $\bar{\eta}, \sigma_\eta, \bar{u}$ and σ_u above the bottom profile, $z_b(x)$, where the data points from the three repeated runs are presented to indicate the degree of reliability of the measurements. The reduction of b increases the wave energy dissipation on the seaward slope of the breakwater and decreases the standard deviation σ_η and wave height $H_{ms} = \sqrt{8}\,\sigma_\eta$. The decreased σ_η leads to the reduction of $|\bar{u}|$ and σ_u. It is noted that the velocity comparisons are not exact because the velocities were measured near the bottom but the numerical model predicts essentially the depth-averaged $\bar{u}$ and σ_u only. The choice of $b = 3$ yields better agreement for σ_η but the overprediction of wave setup, $\bar{\eta}$, is less for $b = 2$.

Figure 2.12 shows the computed cross-shore variations of n, a, Q and σ_*. The ratio n between the group and phase velocities defined in Equation (2.5) is larger than 0.9 and the computation domain is practically in shallow water. The coefficient a in Equation (2.26) and given by Equation (2.27) increases D_B due to intense wave breaking on the seaward slope of the breakwater. The fraction Q of breaking waves increases gradually on the 1/35 slope as more shoaling waves broke as they propagated landward. The steep seaward slope caused all waves to break in the narrow region of $Q = 1$ in this figure. The landward decrease of Q from unity implies that the number of breaking

waves was reduced as more waves ceased breaking on the structure. The parameter σ_* is defined as $\sigma_* = \sigma_\eta / \bar{h}$ for $\sigma_* < \sigma_{*_c} = \gamma / \sqrt{8}$ with $\sigma_{*_c} = 0.25$ for $\gamma = 0.7$. To decrease σ_* in the vicinity of the seaward edge of the structure crest, the empirical adjustment of $\sigma_* = \left(\sigma_{*_c} \sigma_\eta / \bar{h}\right)^{0.5}$ for $\sigma_* > \sigma_{*_c}$ is made to reduce the spatial variation of $\bar{u}, \sigma_u, \bar{v}$ and σ_v in the region of intense wave breaking where linear wave theory is not accurate

Figure 2.13 shows the cross-shore variations of $S_{xx}^* = S_{xx} / \rho g$ and $\tau_b^* = \tau_b / \rho g$ involved in the momentum equation (2.2) where $\tau_b = 0$ is assumed on the smooth 1/35 slope. The time-averaged bottom shear stress is negative because $\bar{u} < 0$ but its magnitude is very small. The cross-shore radiation stress, S_{xx}, decreases due to wave breaking on the structure and causes the wave setup, $\bar{\eta}$, shown in Figure 2.11.

Figure 2.14 shows the cross-shore variations of $\bar{v}$ and σ_v inside the porous structure. The mean discharge velocity, $\bar{v}$, driven by the mean water level gradient in Equation (2.21) is negative (offshore) and much smaller than the return current, $\bar{u}$, above the structure shown in Figure 2.11. The standard deviation σ_v given by Equation (2.25) is of the order of 1 cm/s and much small than σ_u which is of the order of 20 cm/s. The porous structure reduces the fluid velocities considerably.

Figure 2.15 shows the cross-shore variations of $F^* = F / \rho g$, $D_B^* = D_B / \rho g$, $D_r^* = D_r / \rho g$ and $D_f^* = D_f / \rho g$ involved in the energy equation (2.3). The wave energy flux decreases gradually on the 1/35 slope, where some large waves broke, before the rapid decrease on the seaward side of the structure due to intense wave

breaking. The energy dissipation rate, D_B, has been adjusted in the model to simulate the observed wave breaking pattern. The energy dissipation rate, D_r, due to the porous flow resistance inside the structure is much smaller than D_B on the seaward side of the structure but becomes as large as D_B on the landward side of the structure where Q decreases landward as shown in Figure 2.12. The energy dissipation rate, D_f, due to the bottom friction on the structure is of the order of 0.1 D_r and negligible in Equation (2.3) for the case of $f_b = 0.01$.

Figure 2.16 shows the sensitivity to f_b = 0.01 and 0.05 for test R6 where β_o = 5 and γ = 0.7 remain the same and b = 3 in the following. The increase of f_b increases $(-\tau_b)$ in Equation (2.2) and the wave setup, $\bar{\eta}$, on and landward of the structure. On the other hand, the increase of f_b increases D_f in Equation (2.3) but D_f is still small relative to D_B and D_r. The standard deviation σ_η determined mainly by Equation (2.3) does not decrease much. The effects of f_b on $\bar{u}$ and σ_u are also small. It is noted that f_b = 0.05 was a typical value in the time-dependent model by Wurjanto and Kobayashi (1993). The value of f_b = 0.01 is used here as a typical value because the friction factor, f_b, for the time-averaged bottom shear stress, τ_b, was found to be much smaller than f_b for the oscillatory bottom shear stress (Cox and Kobayashi 1997).

Figure 2.17 shows the sensitivity to β_o = 5 and 1 for test R6 where γ = 0.7, b = 3 and f_b = 0.01. For the experiment, α = 0.87 s^{-1}, β_1 = 1.18 cm^{-1} and β_2 = 4.57 s^{-1} in Equation (2.16) for β_0 = 1. The laminar flow resistance coefficient, α, is small relative to the turbulent flow resistance coefficient, β, which is proportional to β_o. Equations (2.21)

and (2.25) suggest that the decrease of β_o increases σ_v and $|\overline{v}|$ because the flow resistance is reduced. The decrease of β_o results in the increase of D_r in Equation (2.19) because the increase of σ_v^3 is larger than the decrease of β. The increase of D_r causes the larger decrease of σ_η, $|\overline{u}|$ and σ_u and the larger increase of $\overline{\eta}$ on the structure. The agreement for $\overline{\eta}$ and σ_η is clearly better for $\beta_o = 5$ than $\beta_o = 1$ which is close to 1.1 recommended by van Gent (1995) on the basis of his water tunnel experiments which are different from the present experiment. Nevertheless, the calibrated value of $\beta_o = 5$ should be regarded to compensate the crude but simple equations (2.19), (2.21) and (2.25).

Figure 2.18 shows the sensitivity to $\gamma = 0.7$ and 0.6 for test R6 where $\beta_o = 5$, $b = 3$ and $f_b = 0.01$. The decrease of γ reduces the depth-limited wave height, H_m, in Equation (2.26) and increases Q and D_B on the seaward 1/35 slope. This increase of D_B in Equation (2.3) results in the decrease of σ_η, $|\overline{u}|$ and σ_v and the increase of $\overline{\eta}$ on the seaward 1/35 slope. However, the wave setup, $\overline{\eta}$, on and landward of the structure is reduced because of the decrease of σ_η on the structure. As a whole, $\gamma = 0.7$ predicts σ_η better and $\gamma = 0.6$ predicts $\overline{\eta}$ better.

Figures 2.19 – 2.21 show the comparisons with the data for tests R4, R8 and R10 with $\gamma = 0.7$ and 0.6 where $\beta_o = 5$, $b = 3$ and $f_b = 0.01$. The agreement for the four tests in Figures 2.18 – 2.21 is similar. The agreement for σ_η is good partly because D_B, D_r and D_f in the energy equation (2.3) can be adjusted through γ, b, β_o and f_b. The numerical model

slightly overpredicts the landward wave setup, $\bar{\eta}$, partly because τ_b in the momentum equation (2.2) can be adjusted directly by f_b alone. This implies that the radiation stress, S_{xx}, given by Equation (2.4) using linear progressive wave theory is not very accurate (Svendsen et al. 2003). However, the numerical model predicts the degree of the change of the landward $\bar{\eta}$ and σ_η caused by the change of the still water depth, d_c, on the crest of the breakwater as listed in Tables 2.5 and 2.6. To improve the agreement for $\bar{u}$ and σ_u, it will be necessary to include the vertical variations of $\bar{u}$ and σ_u and compare the measured and predicted values at the same elevation above the bottom.

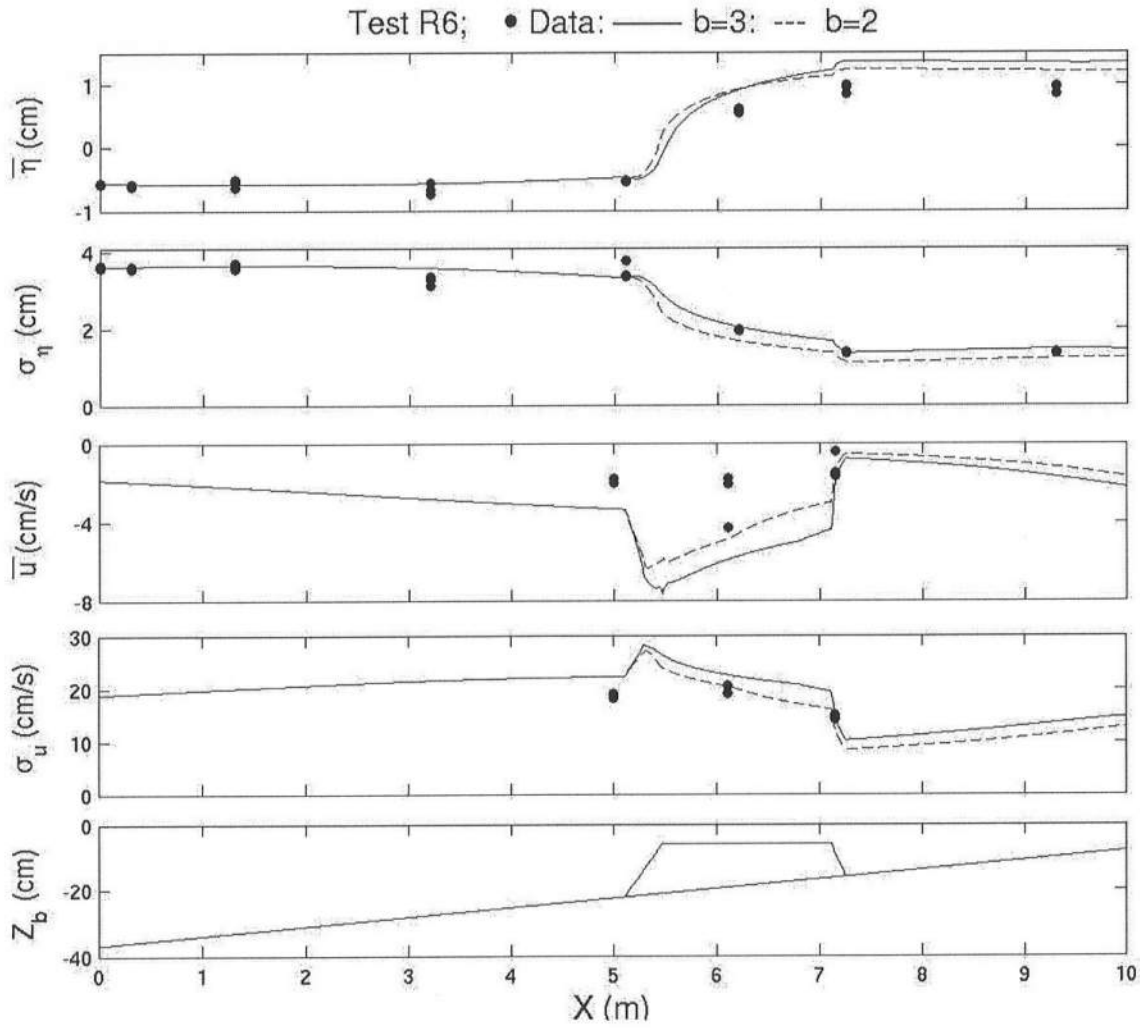

Figure 2.11: Measured and Computed Cross-Shore Variations of Mean and sStandard Deviation of η and u Above Bottom Profile, z_b, for Test R6 with Slope Adjustment Factor, b = 3 and 2

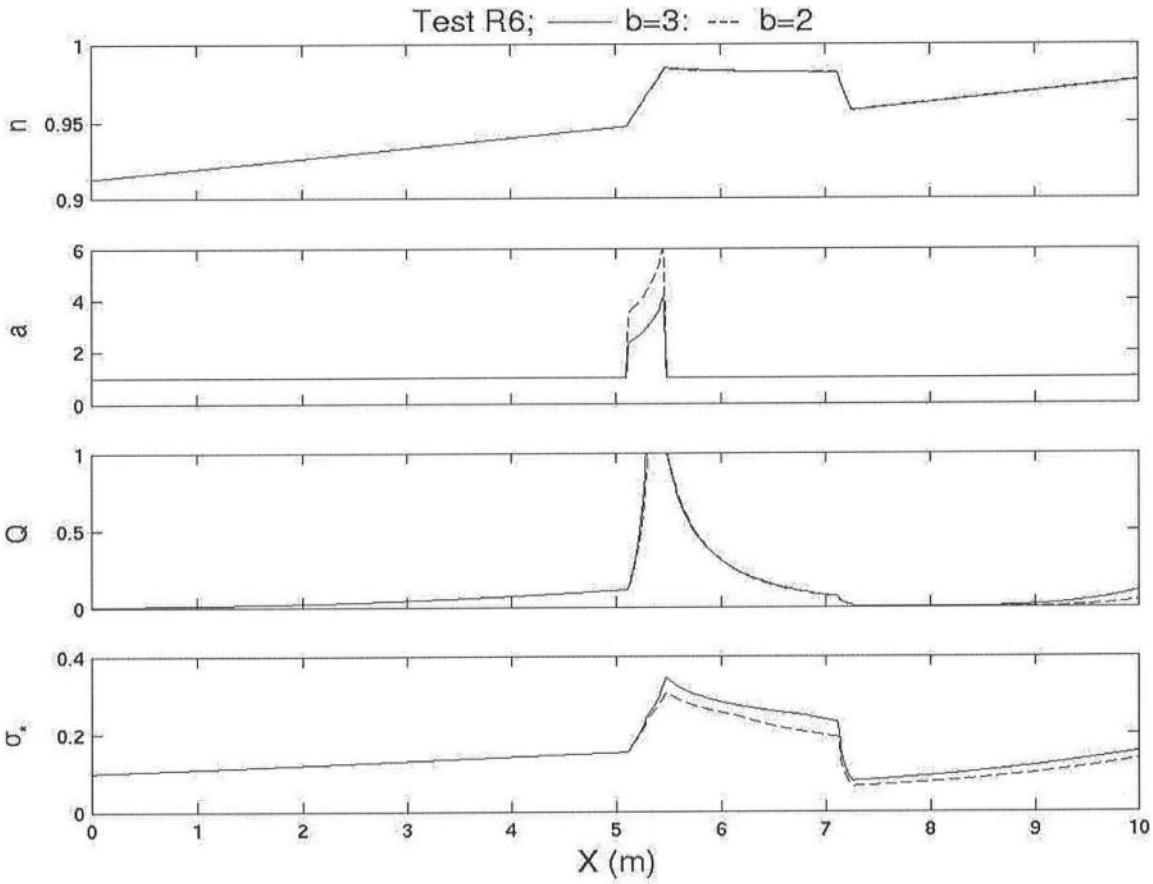

Figure 2.12: Computed Cross-Shore Variations of Wave Shoaling and Breaking Parameters *n, a, Q,* and σ_*

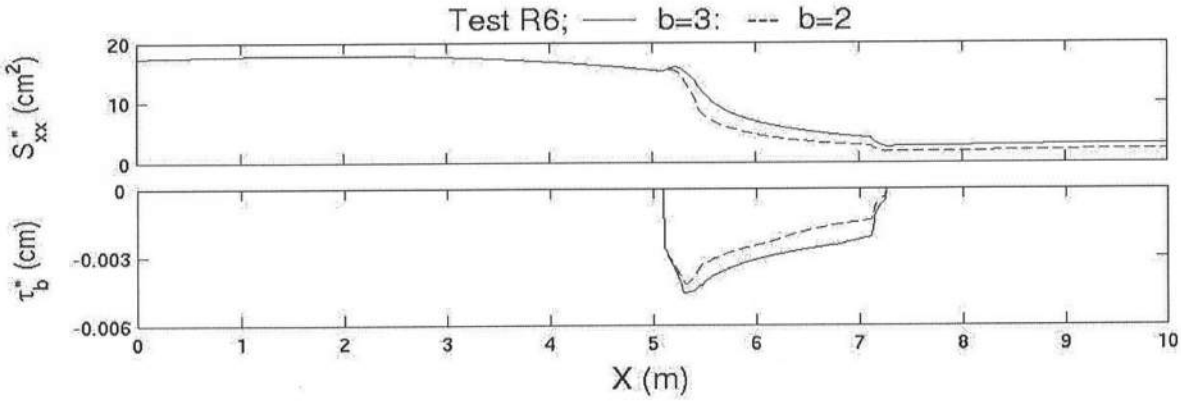

Figure 2.13: Computed Cross-Shore Variations of Radiation Stress, $S_{xx} = \rho g S^*_{xx}$, and Bottom Shear Stress, $\tau_b = \rho g \tau^*_b$

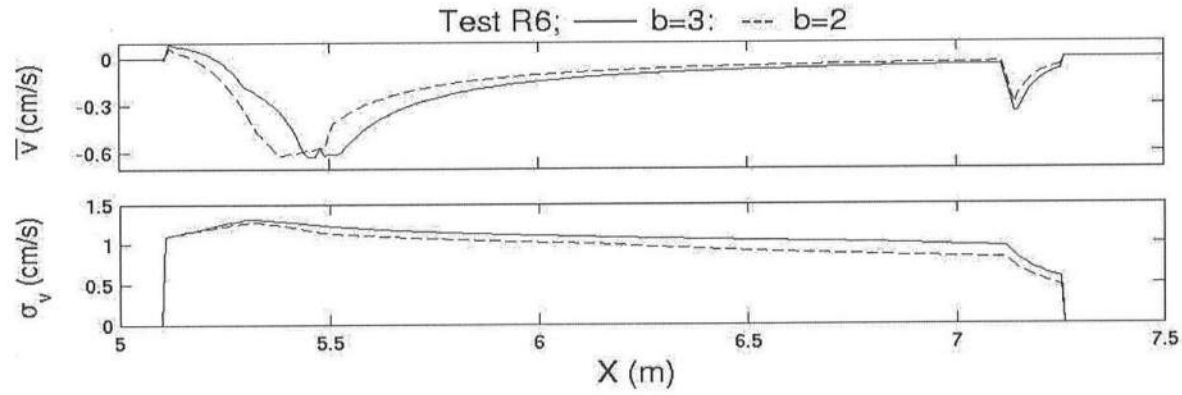

Figure 2.14: Computed Cross-Shore Variations of Mean and Standard Deviation of Horizontal Discharge Velocity, v, Inside Porous Breakwater

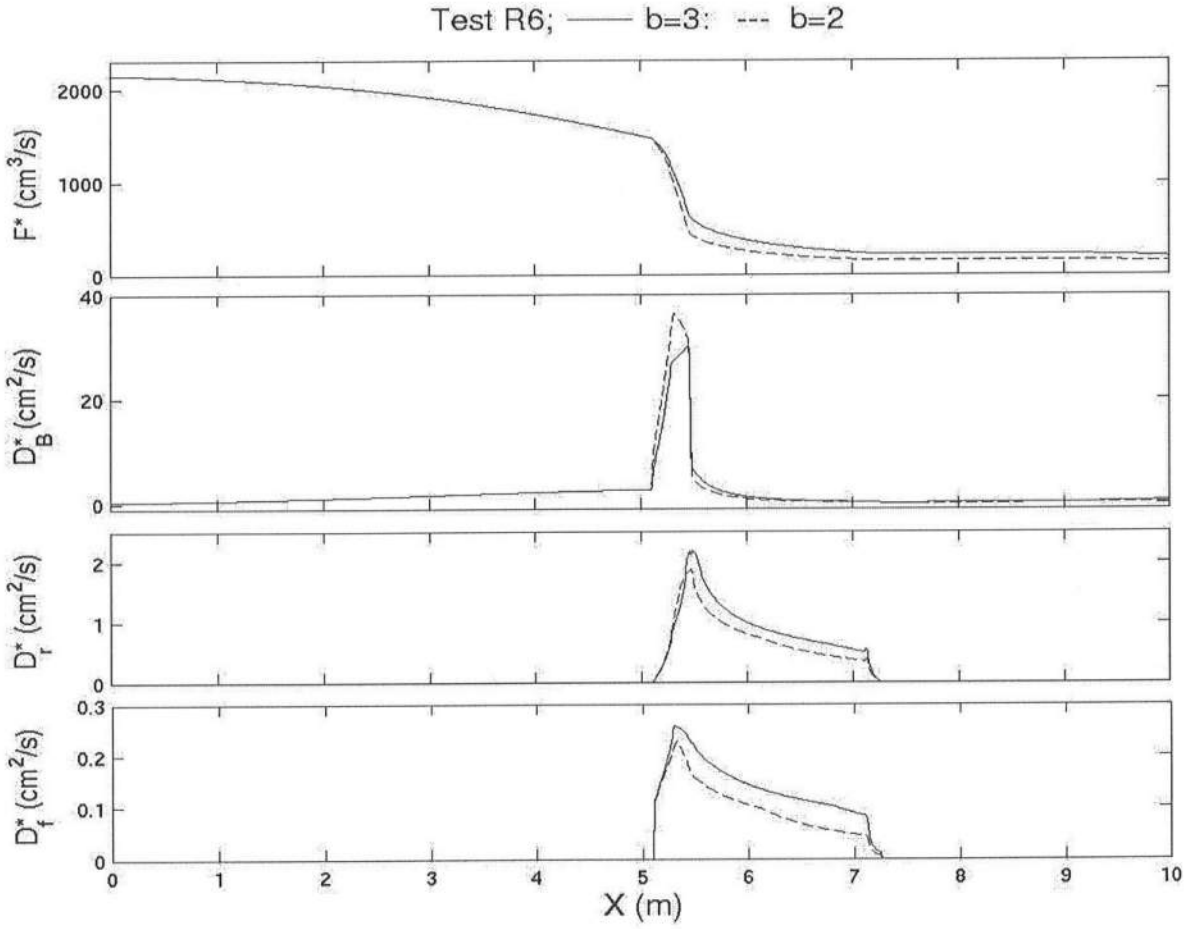

Figure 2.15: Computed Cross-Shore Variations of Wave Energy Flux, $F = \rho g F^*$, and Dissipation Rates, $D_B = \rho g D_B^*$, $D_r = \rho g D_r^*$, and $D_f = \rho g D_f^*$, Due to Wave Breaking, Porous Flow Resistance, and Bottom Friction, Respectively

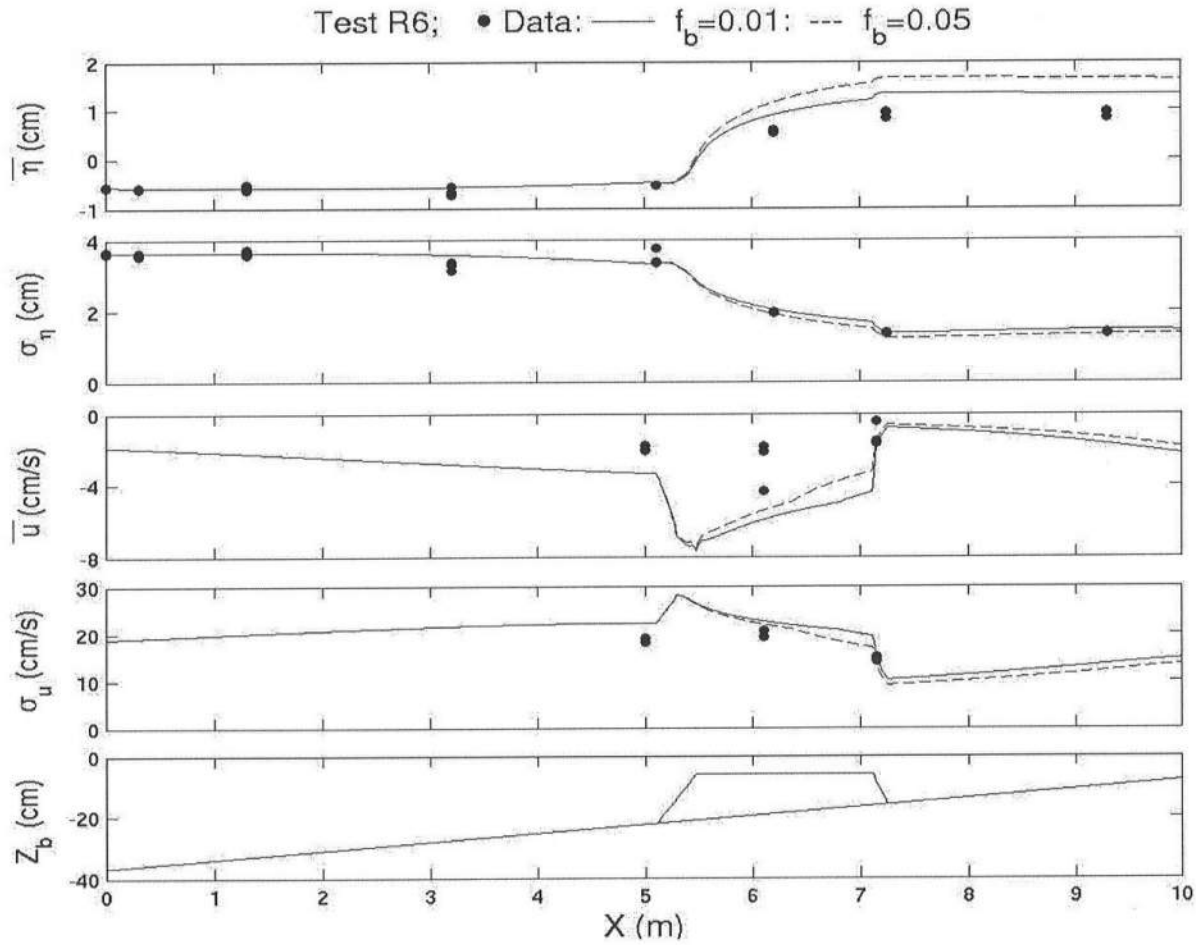

Figure 2.16: Sensitivity to Bottom Friction Factor, f_b = 0.01 and 0.05

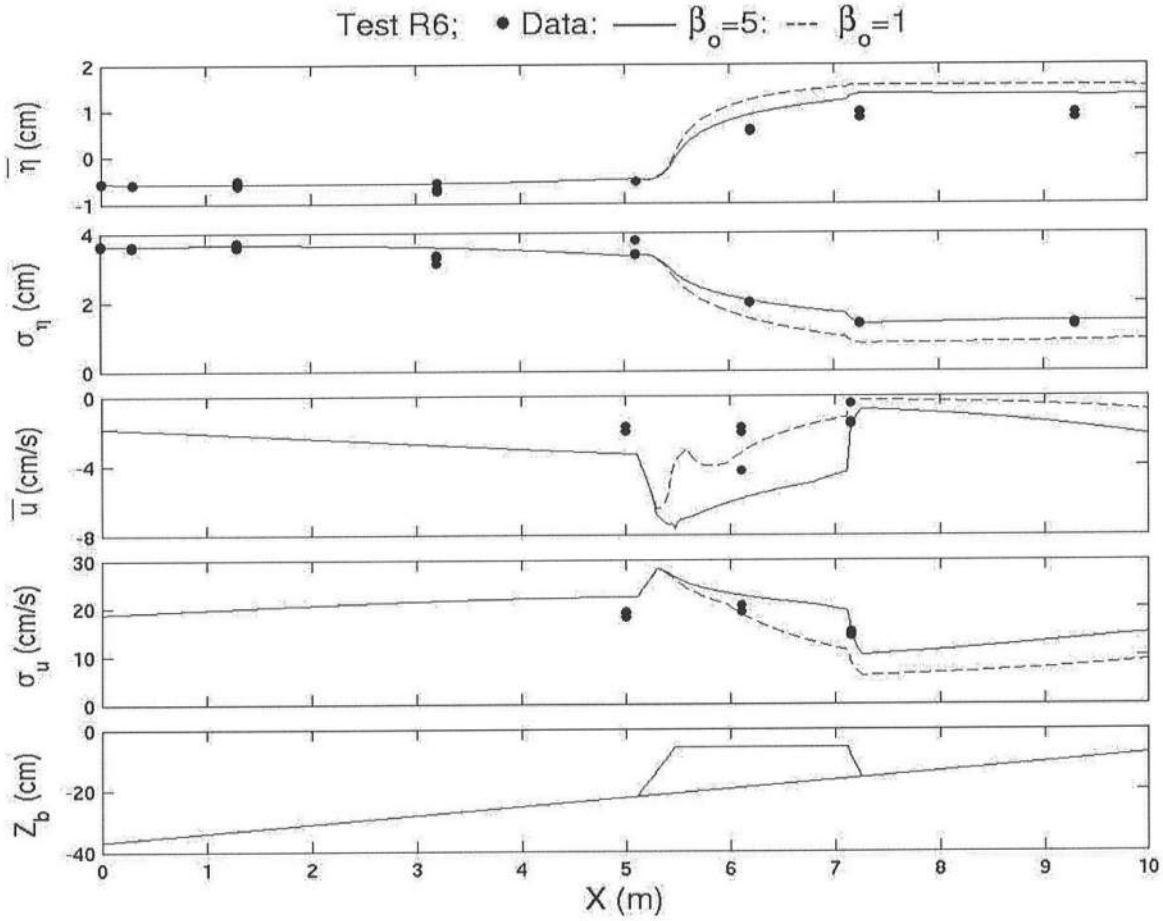

Figure 2.17: Sensitivity to Turbulent Porous Flow Resistance Factor, β_0 = 5 and 1

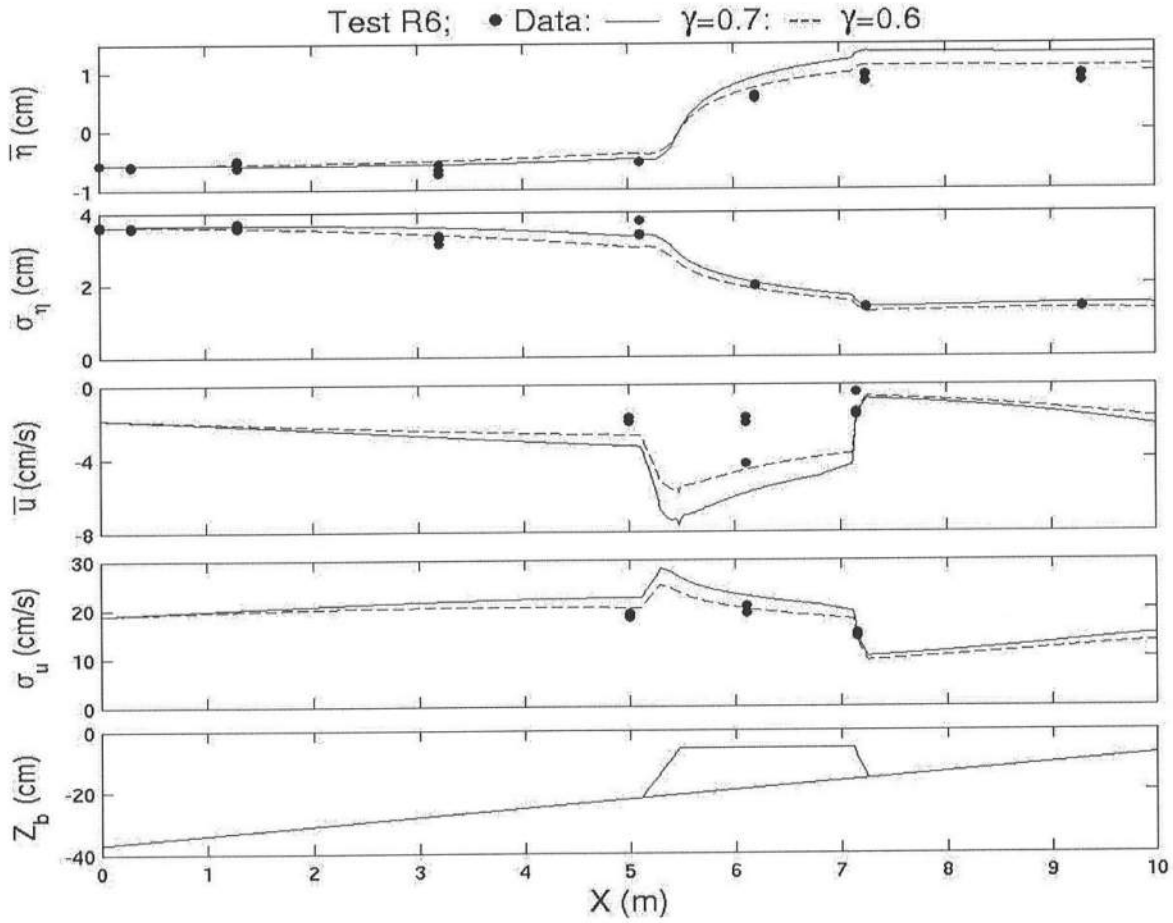

Figure 2.18: Sensitivity to Breaker Ratio Parameter, $\gamma = 0.7$ and 0.6, for Test R6

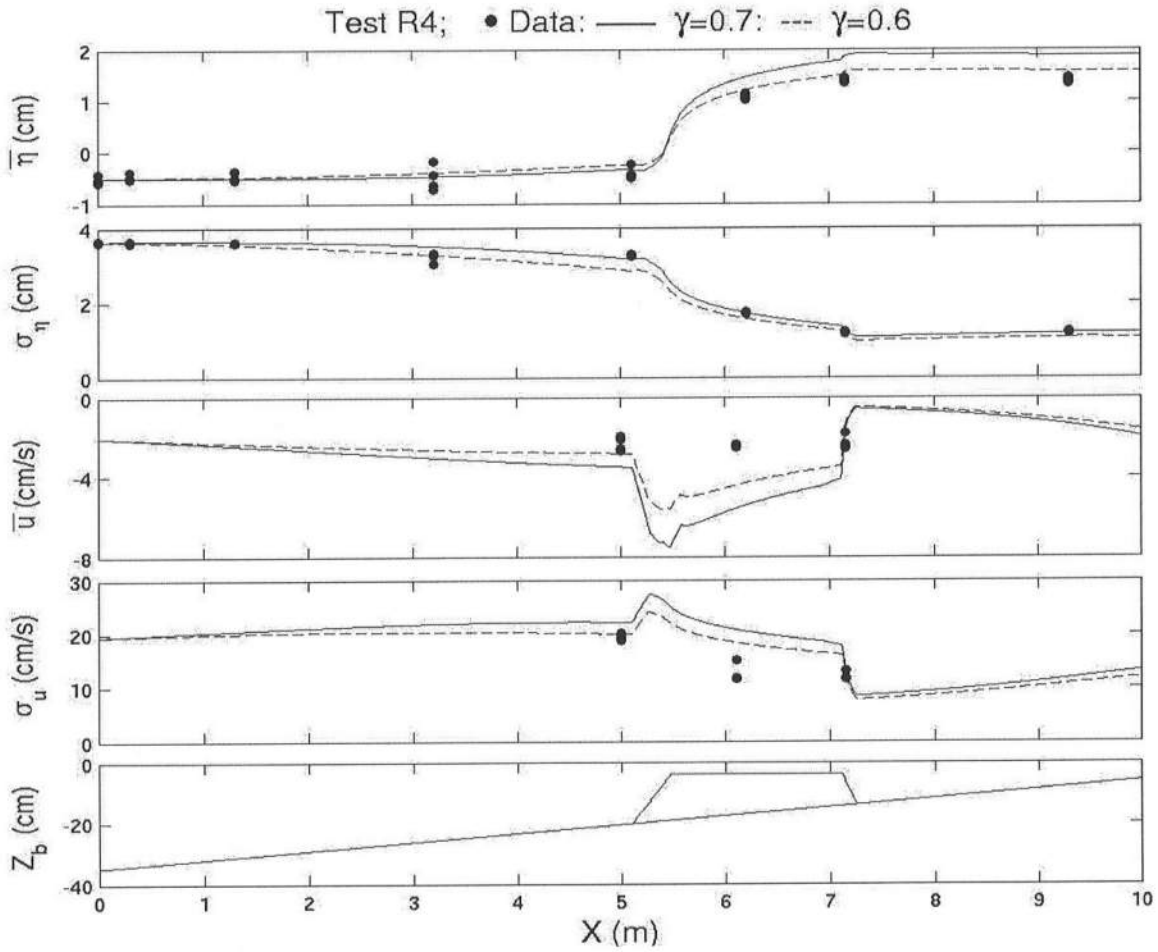

Figure 2.19: Comparison with Data for Test R4

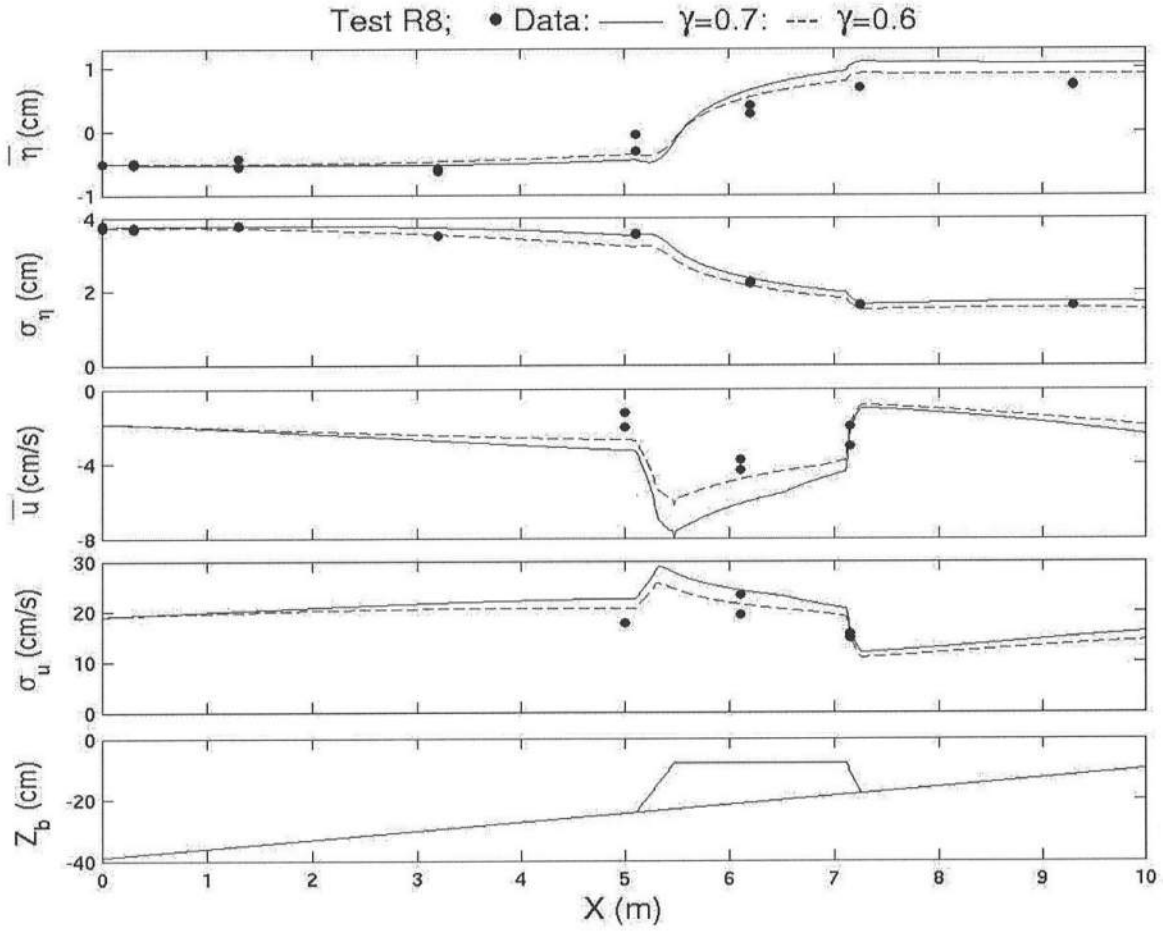

Figure 2.20: Comparison with Data for Test R8

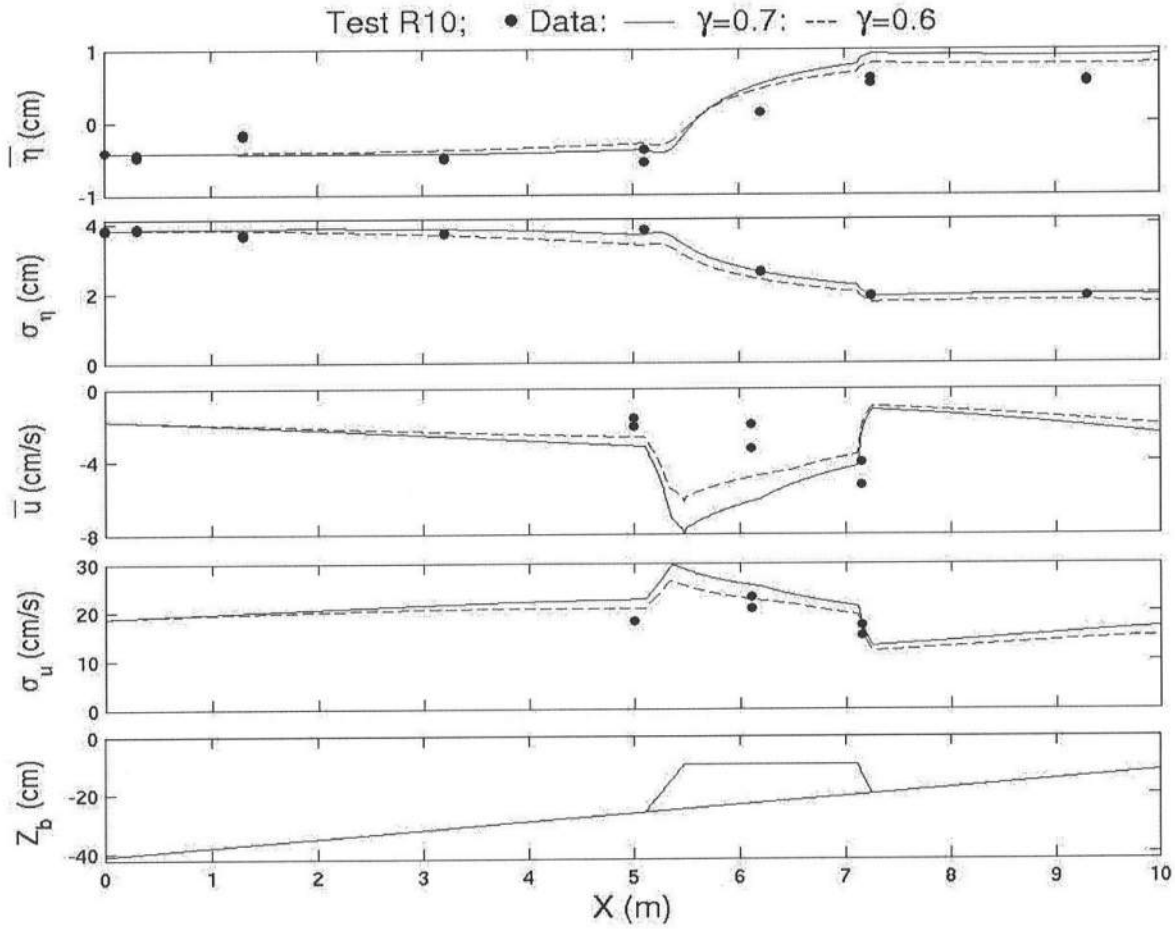

Figure 2.21: Comparison with Data for Test R10

Chapter 3

IRREGULAR BREAKING WAVE TRANSFORMATION ON POROUS REVETMENT

3.1 INTRODUCTION

The time-averaged model called CSHOREP in Chapter 2 is compared with the corresponding time-dependent model PBREAK for the three laboratory tests used to verify PBREAK by Wurjanto and Kobayashi (1993). The computed mean and standard deviation of the free surface elevation and fluid velocities are shown to be comparable, while the computation time is reduced by a factor of 10^{-3}. In the following, the time-dependent model is explained briefly and the comparisons of the two models are then shown for the three tests.

3.2 TIME-DEPENDENT NUMERICAL MODEL PBREAK

Wurjanto and Kobayashi (1993) compared PBREAK with three tests conducted in a wave tank. The still water depth was 40 cm. A layer of gravel was placed on an

impermeable 1/3 slope. The diameter and porosity of the gravel were 2.1 cm and 0.48, respectively. The horizontal width of the gravel layer was 56.6 cm. Measurements were made of irregular wave reflection and runup on the 1/3 gravel slope. The seaward boundary $x = 0$ is located at the toe of the 1/3 gravel slope. The measured incident waves at $x = 0$ were specified as input to PBREAK. The measured reflection coefficients at $x = 0$ for the three tests were about 0.2 where wave reflection is neglected in the time-averaged model CSHOREP. The time-dependent model PBREAK was capable of predicting the time series of the reflected waves at the toe of the 1/3 slope and the shoreline oscillations on the slope. No measurement was made of the free surface elevation, η, and the horizontal velocity, u, above the 1/3 slope and the horizontal discharge velocity, v, inside the porous layer.

PBREAK used the laminar and turbulent flow resistance coefficients, α and β, expressed as (Madsen and White, 1975)

$$\alpha = 1140 \frac{\left(1-n_p\right)^3}{n_p^2} \frac{\nu}{D_{n50}^2} \quad ; \quad \beta = 2.7 \frac{\left(1-n_p\right)}{n_p^3 D_{n50}} \tag{3.1}$$

where n_p = porosity of the stone, stone; ν = kinematic viscosity of the fluid; and D_{n50} = nominal stone diameter. Consequently Equations (2.16) ad (2.17) are replaced by Equation (3.1). Correspondingly, Equation (2.21) is rewritten as

$$-g\frac{d\bar{\eta}}{dx}=\bar{v}(\alpha+1.64\beta\sigma_v) \tag{3.2}$$

The rest of the equations in Chapter 2 are not modified in the following computations.

3.3 COMPARISON WITH TIME-DEPENDENT MODEL

CSHOREP is compared with the mean and standard deviation of the time series of η, u and v computed by PBREAK. Table 3.1 lists the values of T_p, $H_{rms} = \sqrt{8}\ \sigma_\eta$ and $\bar{\eta}$ at $x = 0$ and the bottom friction factor, f_b, used as input to CSHOREP. The time series

Table 3.1 Input to Time-Averaged Model

Test	T_p(s)	H_{rms} (cm)	$\bar{\eta}$ (cm)	f_b
P1	1.18	4.71	0.08	0.05
P2	2.12	4.08	0.06	0.05
P3	2.75	3.08	0.06	0.10

of η at $x = 0$ computed by PBREAK is used to obtain the listed values at $x = 0$, whereas the value of f_b calibrated for PBREAK is used for CSHOREP as well. The coefficients α and β given in Equation (3.1) are the same for both models. For $D_{n50} = 2.1$ cm and $n_p = 0.48$, $\alpha = 1.58$ s^{-1} and $\beta = 6.05$ cm^{-1}. The additional empirical parameters included in CSHOREP are γ in Equation (2.26) and b in Equation (2.27). Use is made of $\gamma = 0.7$ and $b = 3$ calibrated Chapter 2 for the submerged porous breakwater in the surf zone on the

impermeable 1/35 slope. In the following, the detailed results for test P2 are presented first. Second, the comparisons for tests P1 and P3 are shown.

Figure 3.1 shows the cross-shore variations of $\bar{\eta}$, σ_η, $\bar{u}$, σ_u, $\bar{v}$ and σ_v computed by CSHOREP and PBREAK for test P2 along with the upper and lower boundaries of the porous layer whose horizontal width was 0.566 m. PBREAK includes the region where the free surface is inside the porous layer. This porous region is not included in CSHOREP. The time series of the instantaneous water depth, $h = (\eta - z_b)$, above the bottom elevation, z_b, computed by PBREAK is used to obtain the mean $\bar{\eta} = \left(\bar{h} + z_b\right)$ and the standard deviation, $\sigma_h = \sigma_\eta$, for the instantaneous free surface elevation, η, above z_b because $h = 0$ when the free surface is inside the porous layer. The wave setup, $\bar{\eta}$, computed by CSHOREP agrees with the wave setup $\left(\bar{h} + z_b\right)$ above the bottom computed by PBREAK. The standard deviation σ_η computed by CSHOREP is smaller near the still water shoreline located at $x = 1.2$ m than σ_h and σ_η computed by PBREAK. On the other hand, the horizontal velocity, u, above the bottom is defined in the same way for both models. The mean current, $\bar{u}$, is offshore (negative) but onshore (positive) near the shoreline because of the seepage into the porous layer. The onshore current, $\bar{u}$, near $x =$ 1.2 m predicted by CSHOREP is too large because of the very small $\bar{h}$ in Equation (2.14). The mean current, $\bar{v}$, in the porous layer driven by the mean water level gradient in Equation (3.1) is offshore (negative) but relatively small even near the shoreline at $x =$

1.2 m. The standard deviation σ_v is of the order of 1 cm/s and much small than σ_u which is of the order of 10 cm/s.

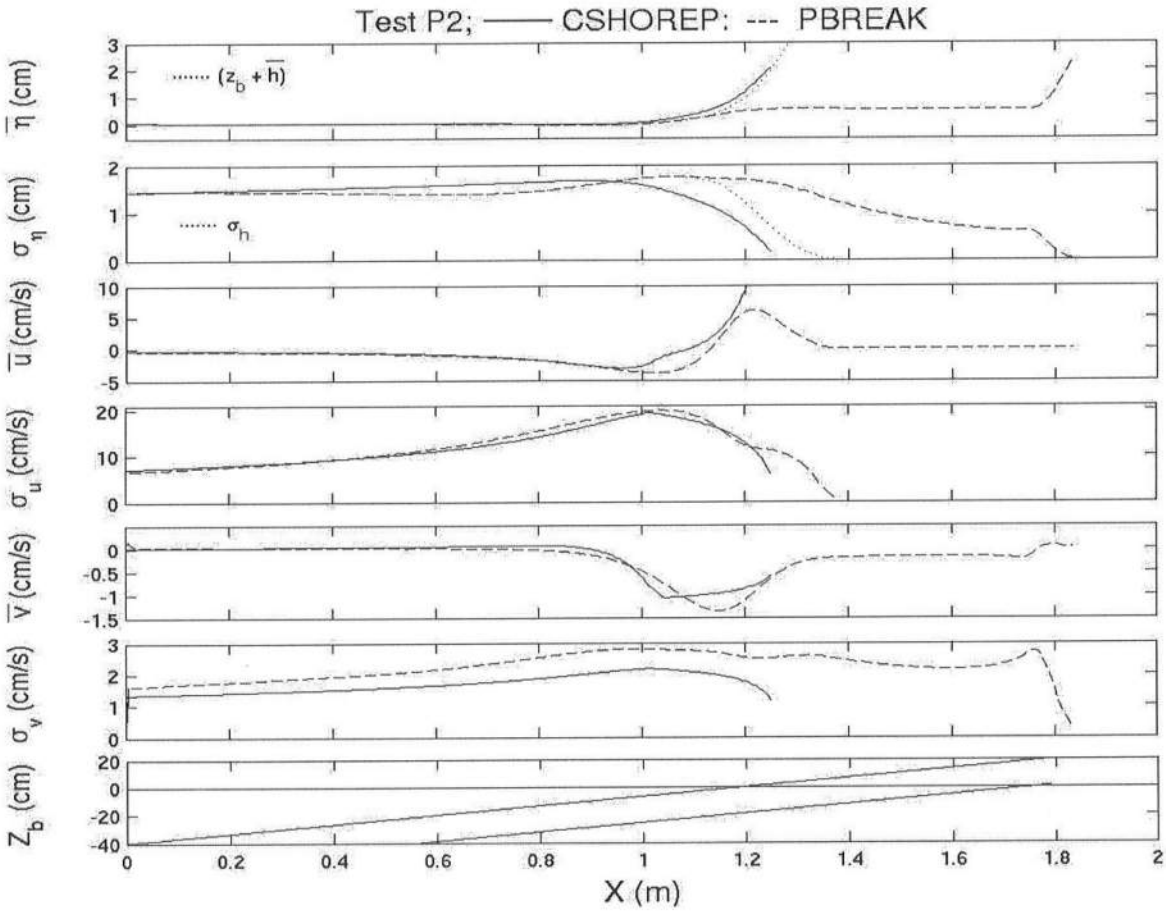

Figure 3.1: Comparisons of Mean and Standard Deviation of Free Surface Elevation, η, Horizontal Fluid Velocity, u, and Horizontal Discharge Velocity, v, Inside Porous Layer for Test P2 Along with Upper and Lower Boundaries of Porous Layer

Figure 3.2 shows the cross-shore variation of n, a and Q for test P2 computed by CSHOREP. The ratio n between the group and phase velocities defined in Equation (2.5) is larger than approximately 0.9 and the computation domain is practically in shallow water. It is noted that $n > 0.7$ for test P1 with $T_p = 1.18$ s as listed in Table 3.1. The coefficient a in Equation (2.26) and given by Equation (2.27) increases landward with the decrease of $\bar{h}$ and significantly increases D_B near the shoreline at $x = 1.2$ m. The fraction Q of breaking waves indicates no wave breaking in the region $x < 0.8$ m and the breaking of all waves in the region $x > 1.0$ m.

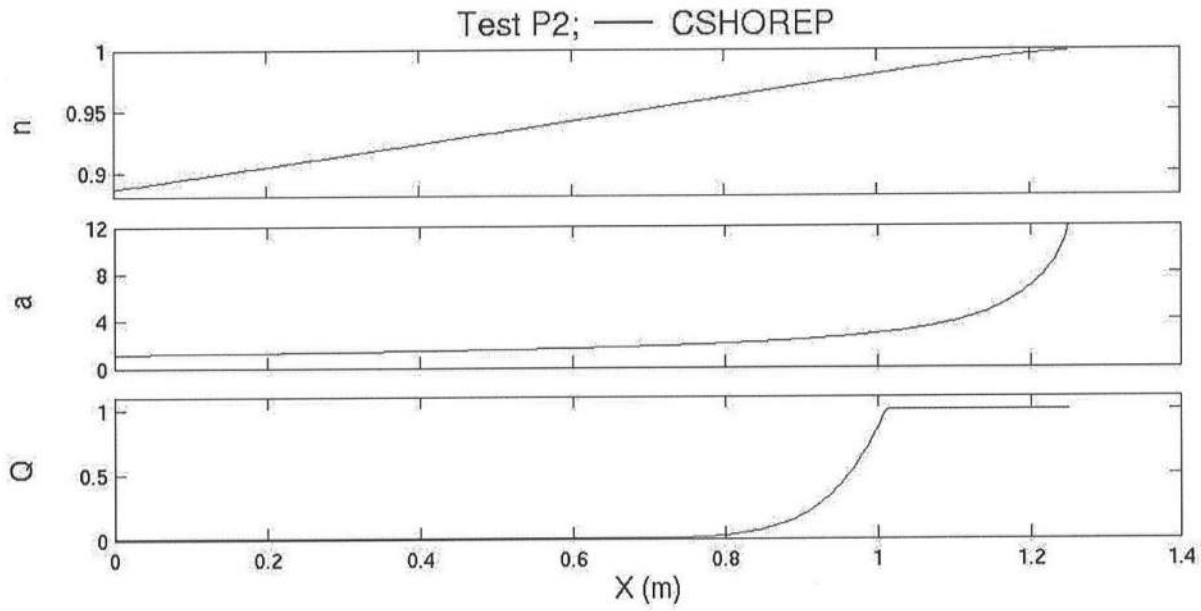

Figure 3.2: Cross-Shore Variations of Wave Shoaling and Breaking Parameters, n, a and Q, Computed by Time-Averaged Model CSHOREP

Figure 3.3 shows the cross-shore variations of $S_{xx}^{*} = S_{xx} / \rho g$ and $\tau_b^{*} = \tau_b / \rho g$ involved in the momentum equation (2.2). The time-averaged bottom shear stress is negative because $\bar{u} < 0$ except near the shoreline at x = 1.2 m and the negative τ_b increases the wave setup, $\bar{\eta}$. The cross-shore radiation stress, S_{xx}, increases landward because of the increase of σ_η in Figure 3.1 due to wave shoaling and decreases rapidly in the region of $Q = 1$ in Figure 3.2.

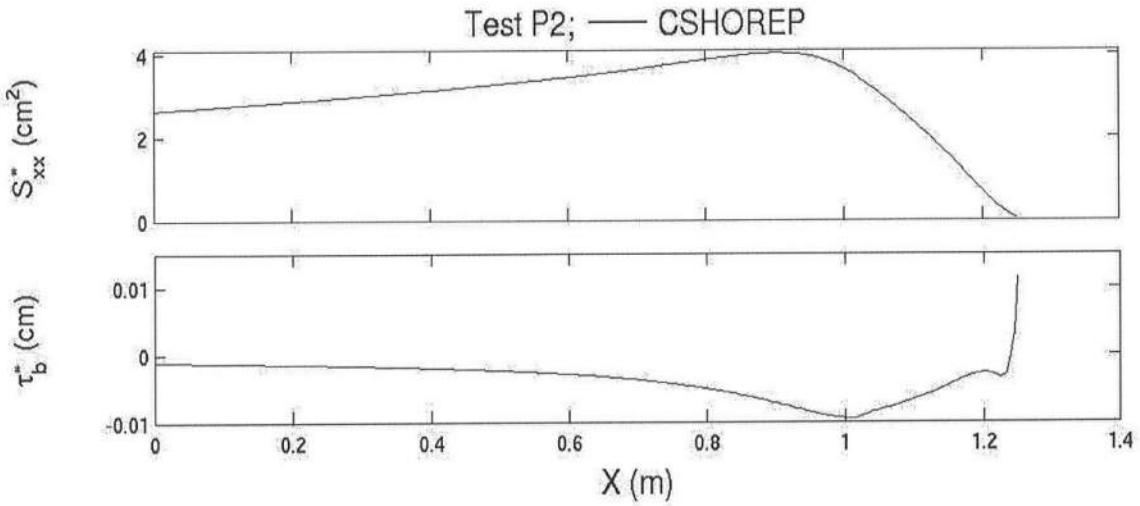

Figure 3.3: Cross-Shore Variations of Radiation Stress, $S_{xx} = \rho g S_{xx}^{*}$, and Bottom Shear Stress, $\tau_b = \rho g \tau_b^{*}$, Computed by CSHOREP

Figure 3.4 shows the cross-shore variations of $F^* = F/\rho g$, $D_B^* = D_B/\rho g$, $D_r^* = D_r/\rho g$ and $D_f^* = D_f/\rho g$ involved in the energy equation (2.3). The wave energy flux, F, decreases gradually outside the surf zone ($x < 0.8$m) and more rapidly in the region $Q = 1$ ($x > 1.0$ m). The energy dissipation rate, D_B, due to wave breaking is large in the surf zone. The energy dissipation rate, D_r, due to the porous flow resistance inside the porous layer increases gradually from the toe of the slope at x =0 and becomes as large as $D_B/2$ near x = 1 m before its landward decrease where D_r given by Equation (2.19) depends on σ_v and $\bar{v}$ shown in Figure 3.1. The energy dissipation rate, D_f, due to the bottom friction is of the order of 0.1 D_r and negligible in Equation (2.3).

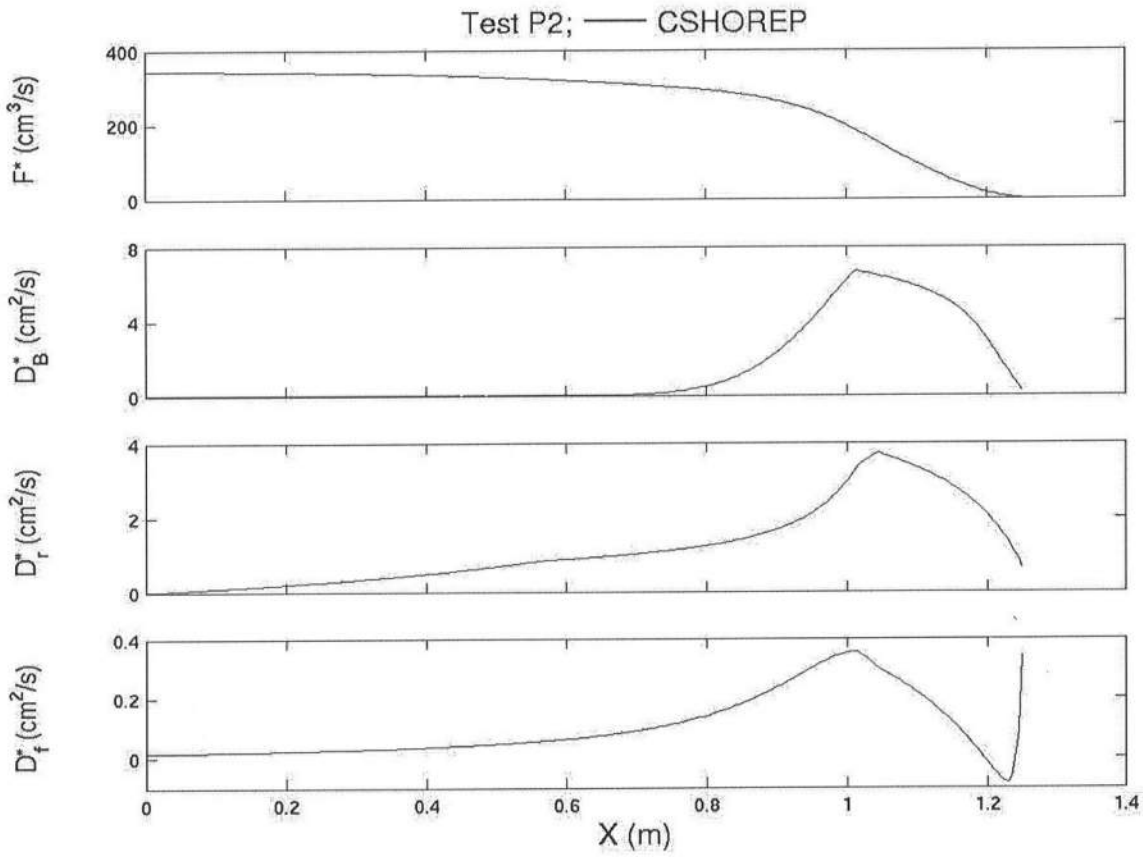

Figure 3.4: Cross-Shore Variations of Wave Energy Flux, $F = \rho g F^*$, and Dissipation Rates, $D_B = \rho g D_B^*$, $D_r = \rho g D_r^*$, and $D_f = \rho g D_f^*$, Due to Wave Breaking, Porous Flow Resistance, and Bottom Friction, Respectively, Computed by CSHOREP

Figures 3.5 - 3.12 show the comparisons between CSHOREP and PBREAK for tests P1 and P3, respectively, in the same way as the figures for test P2. As a whole, the agreement of the two models is good in spite of the various approximations made in CSHOREP and the use of $\gamma = 0.7$ and $b = 3$ calibrated for the different experiment involving the submerged porous structure in Chapter 2. However, CSHOREP will need to be extended to the region where the free surface is inside the porous layer.

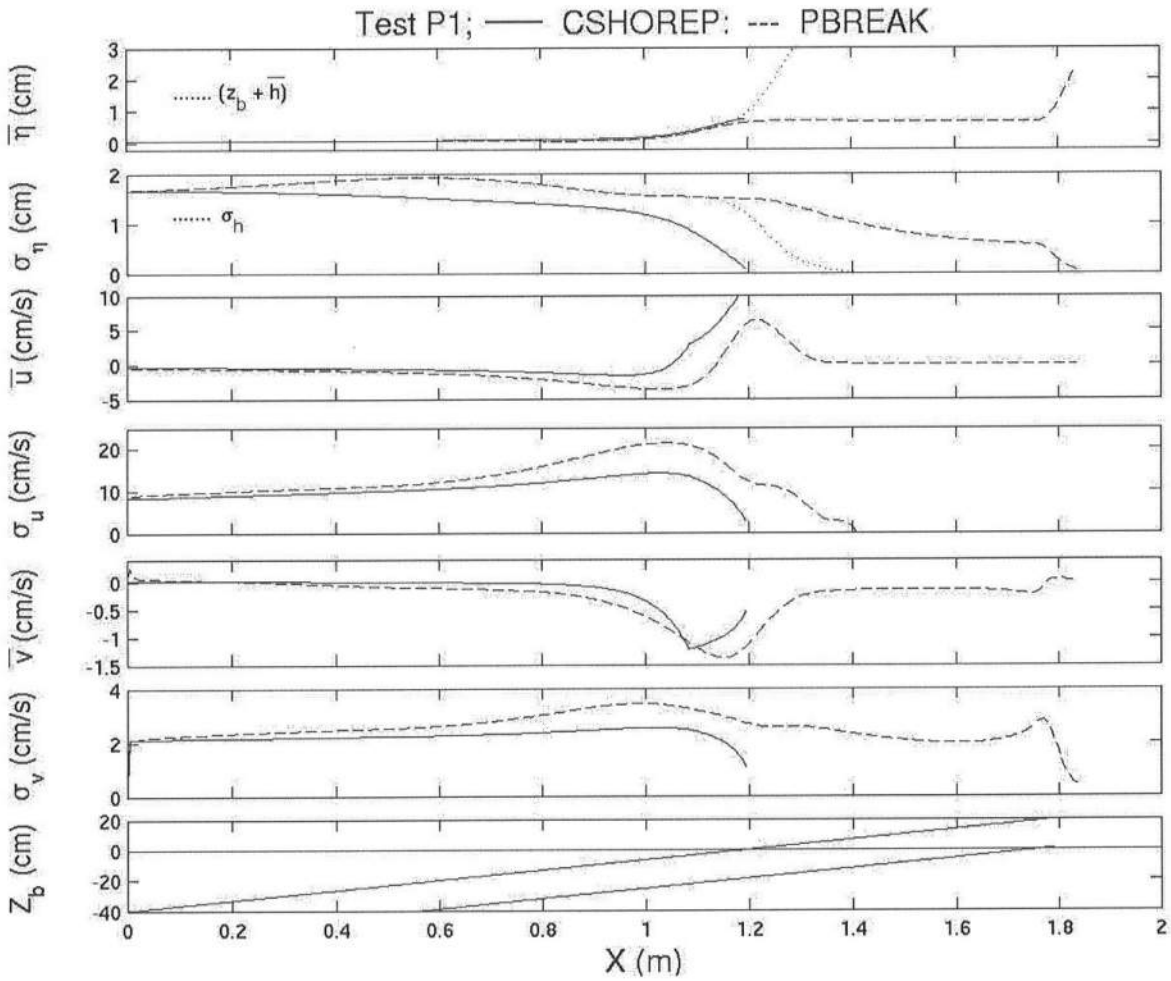

Figure 3.5: Comparisons Between CSHOREP and PBREAK for Test P1

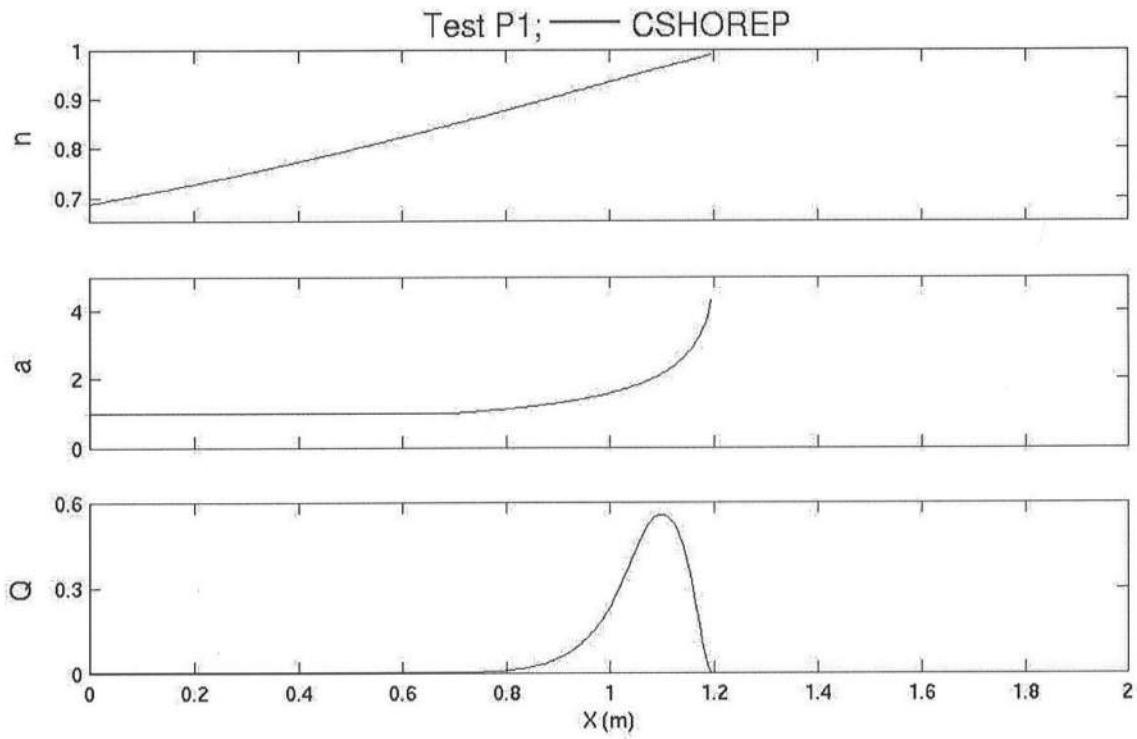

Figure 3.6: Cross-shore Variations of Wave Shoaling and Breaking Parameters, *n, a* and *Q*, Computed by CSHOREP for Test P1

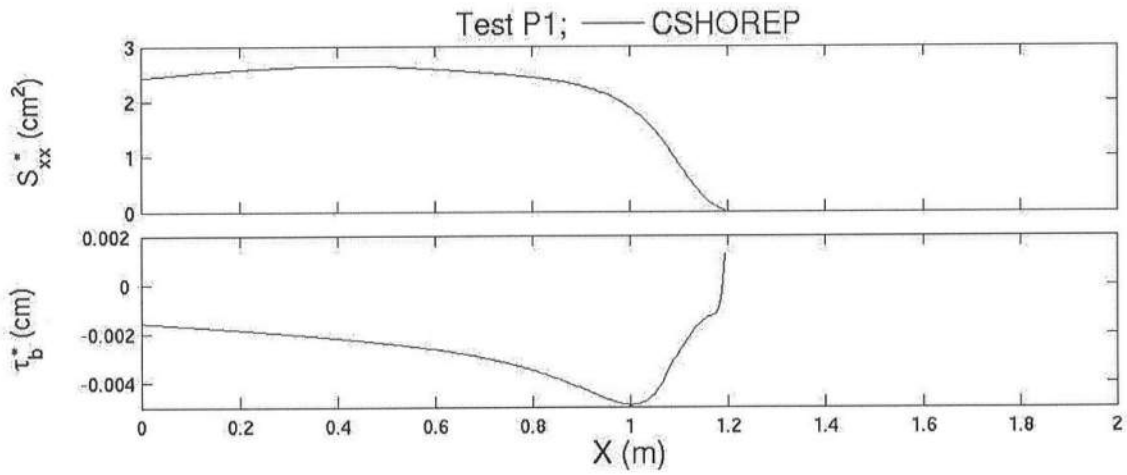

Figure 3.7: Cross-Shore Variations of Radiation Stress, $S_{xx} = \rho g S^*_{xx}$, and Bottom Shear Stress $\tau_b = \rho g \tau^*_b$ Computed by CSHOREP for Test P1

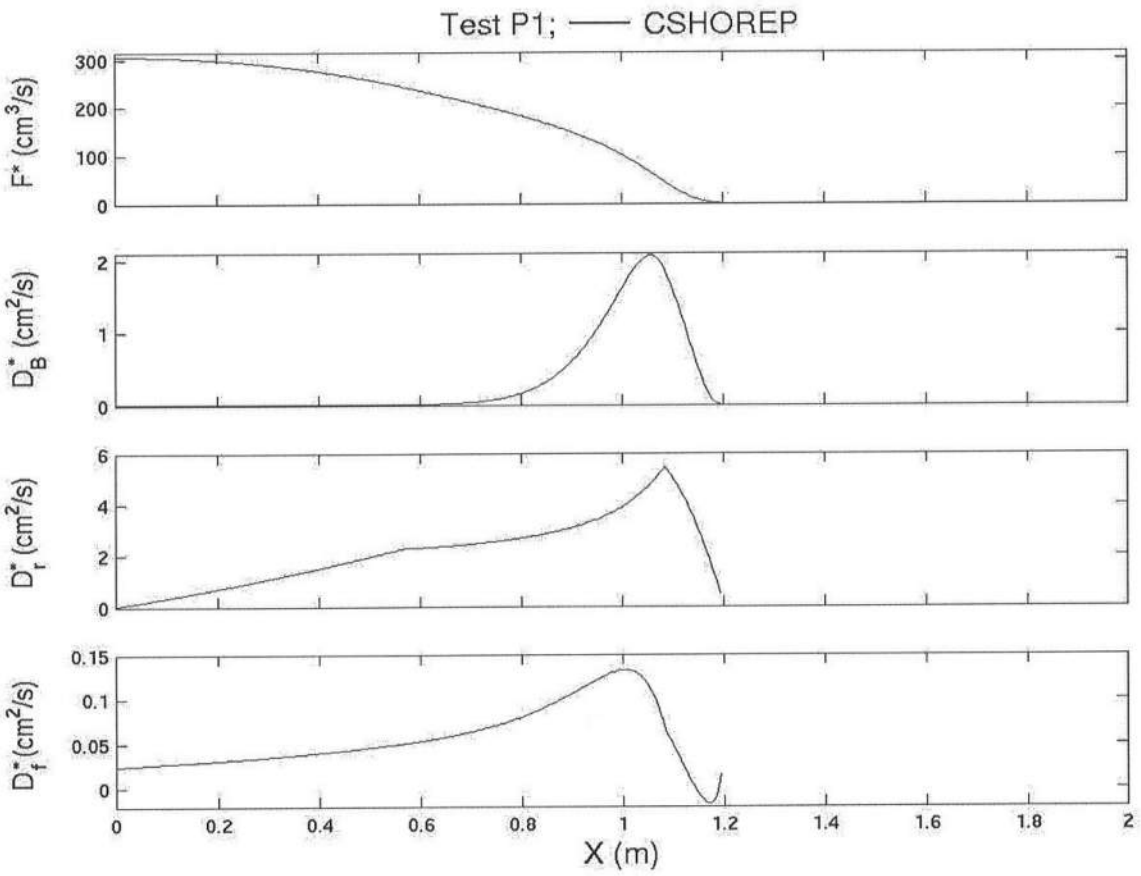

Figure3.8: Cross-Shore Variations of Wave Energy Flux, $F = \rho g F^*$, and Dissipation Rates, $D_B = \rho g D_B^*$, $D_r = \rho g D_r^*$, and $D_f = \rho g D_f^*$, Due to Wave Breaking, Porous Flow Resistance, and Bottom Friction, Respectively, Computed by CSHOREP for Test P1

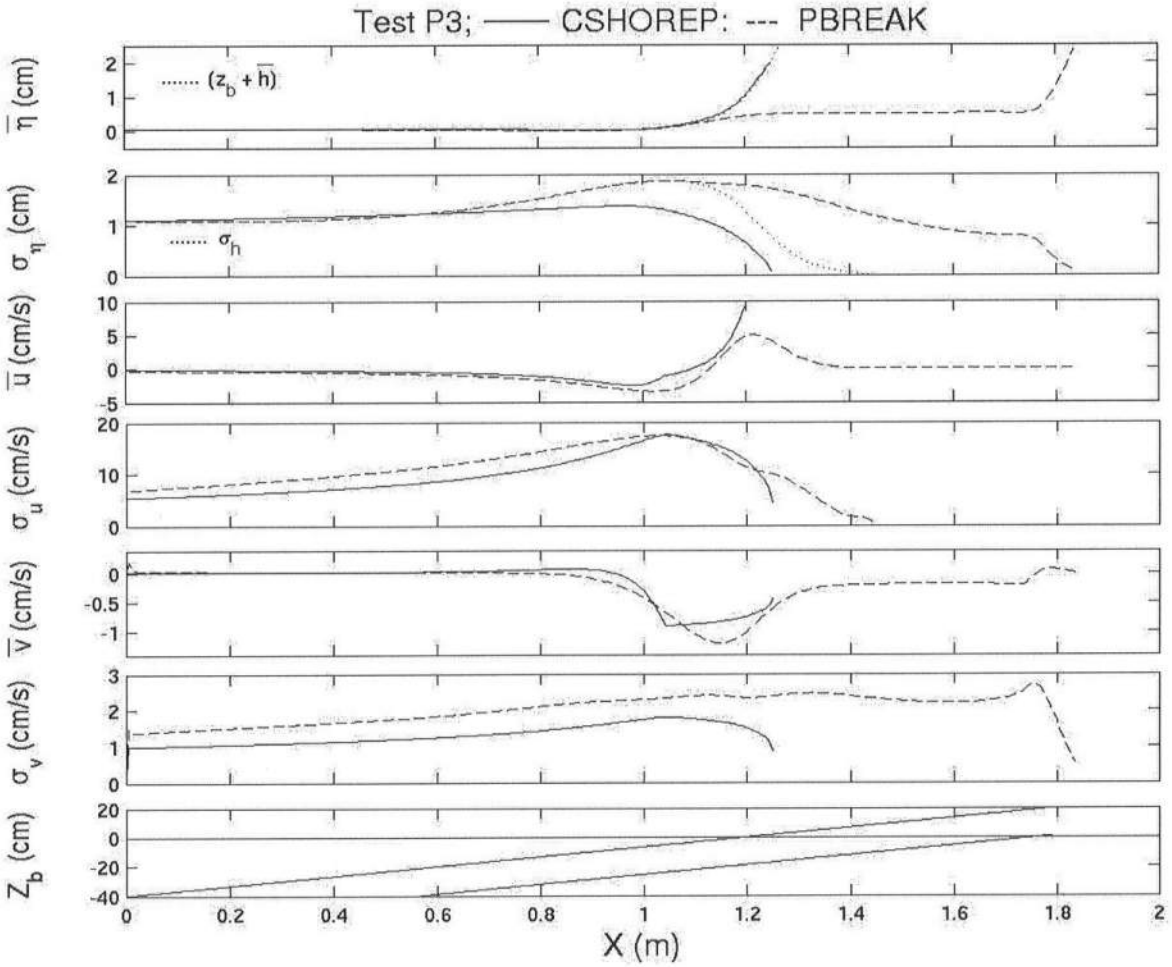

Figure 3.9: Comparisons Between CSHOREP and PBREAK for Test P3

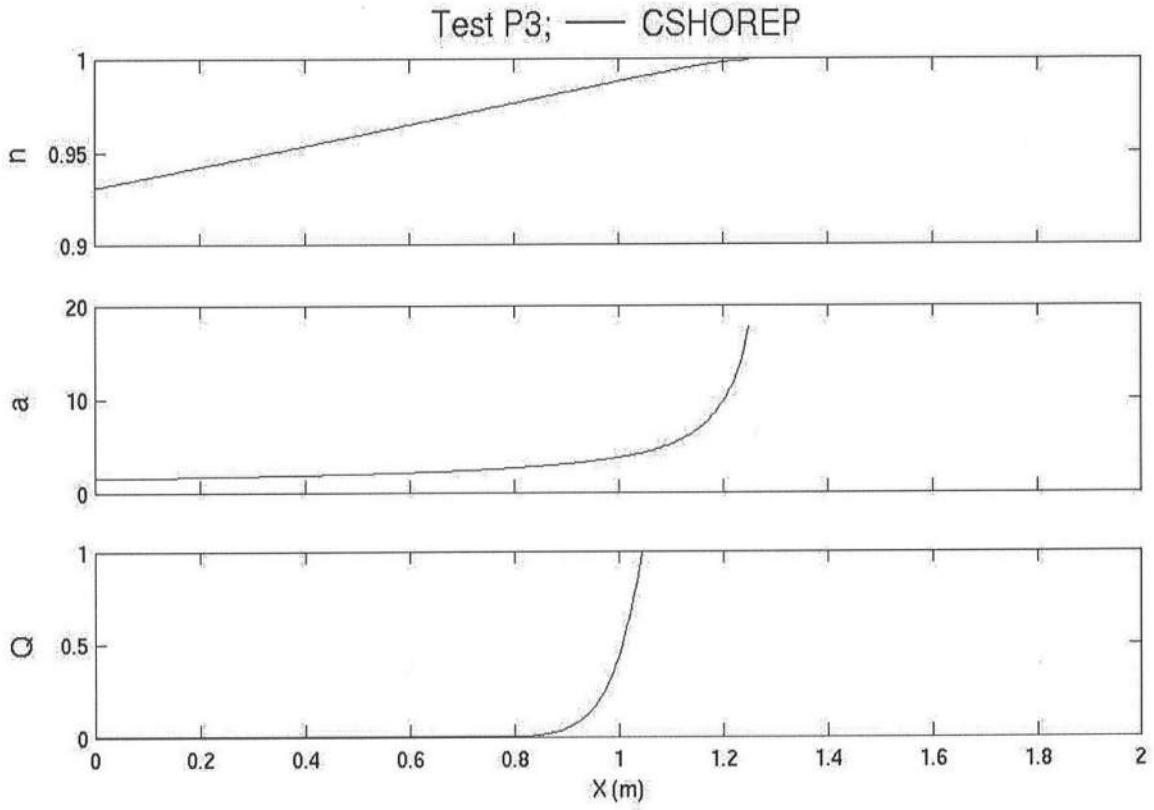

Figure 3.10: Cross-Shore Variations of Wave Shoaling and Breaking Parameters *n, a* and *Q* Computed by CSHOREP for Test P3

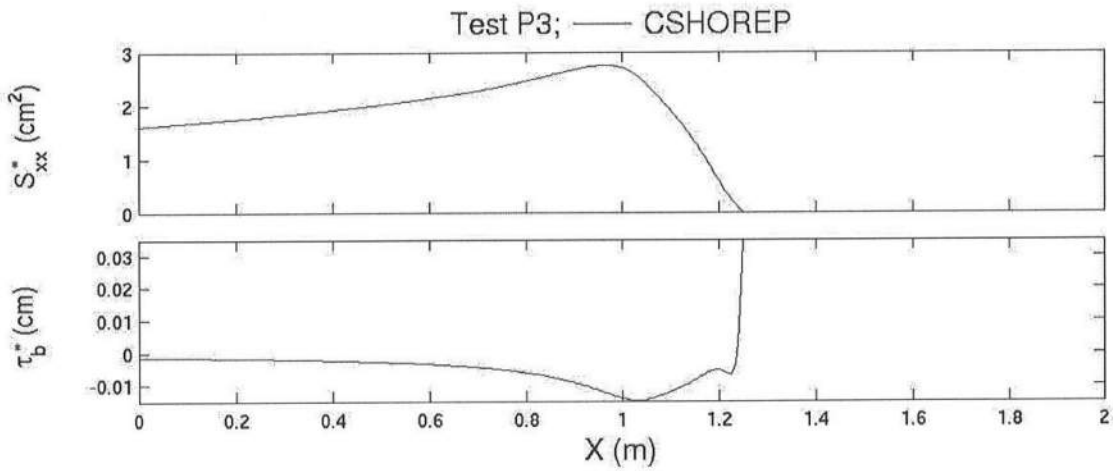

Figure 3.11: Cross-Shore Variations of Radiation Stress, $S_{xx} = \rho g S^*_{xx}$, and Bottom Shear Stress, $\tau_b = \rho g \tau^*_b$, Computed by CSHOREP for Test P3

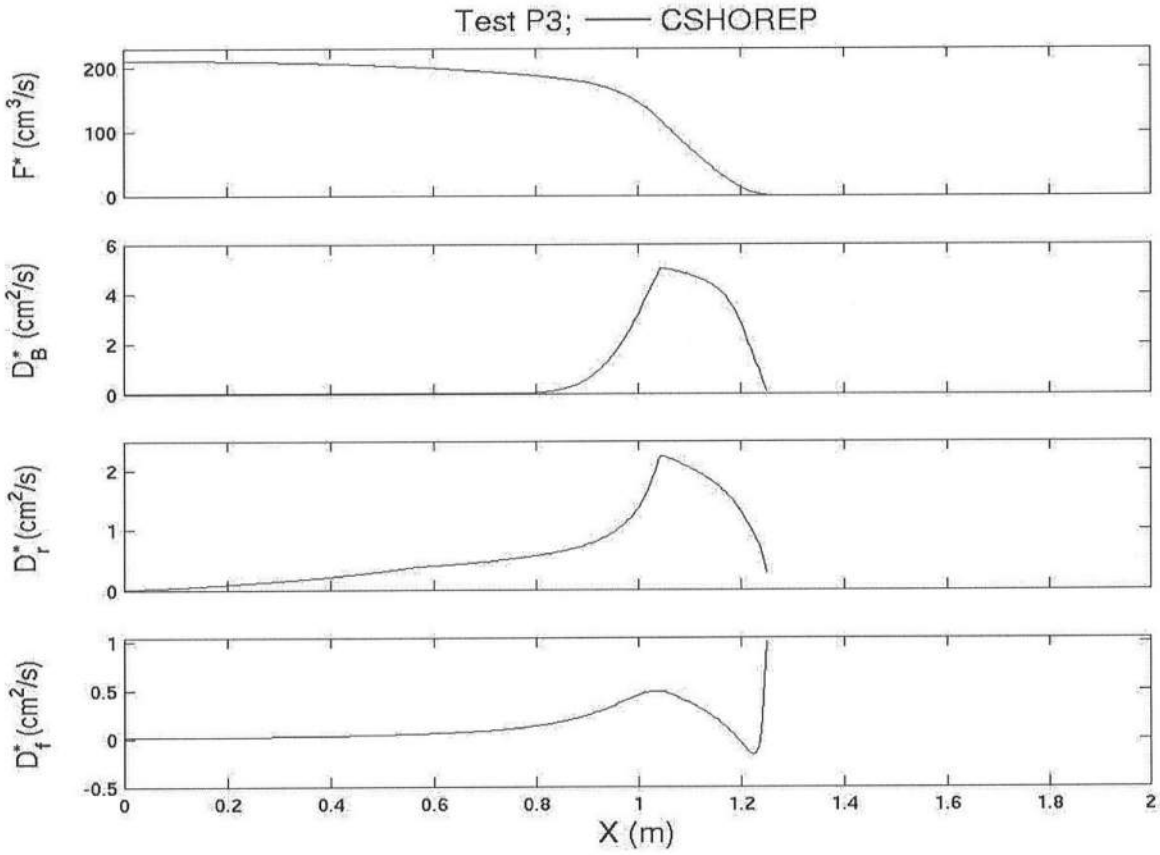

Figure 3.12: Cross-Shore Variations of Wave Energy Flux, $F = \rho g F^*$, and Dissipation Rates, $D_B = \rho g D_B^*$, $D_r = \rho g D_r^*$, and $D_f = \rho g D_f^*$, Due to Wave Breaking, Porous Flow Resistance, and Bottom Friction, Respectively, Computed by CSHOREP for Test P3

Chapter 4

CONCLUSIONS

A numerical model based on time-averaged continuity, momentum and energy equations is developed to predict the mean and standard deviation of the free surface elevation and horizontal fluid velocities above and inside a porous submerged breakwater with a relatively wide crest. The energy dissipation rate due to irregular breaking waves is estimated using the formula of Battjes and Stive (1985) which is modified to increase the dissipation rate on the steep seaward slope in shallow water and account for the reduced wave breaking on the crest and landward slope. Four laboratory tests were conducted by varying the still water depth on a wide-crested breakwater. Data collected during the laboratory experiment include wave setup, wave height, and velocity data. Four empirical parameters associated with irregular wave breaking, porous flow resistance and bottom friction are calibrated using these tests. The calibrated numerical model predicts the cross-shore variations of the mean and standard deviation of the measured free surface elevation and horizontal velocity reasonably well. However, the numerical model will need to be compared with additional experiments.

This time-averaged model is also compared with the corresponding time-dependent model by Wurjanto and Kobayashi (1993) which was verified using three tests for irregular wave runup on a 1/3 revetment slope with a thick porous layer. The cross-shore variations of the mean and standard deviation of the free surface elevation and fluid velocities computed by the two models are shown to be in agreement for the three tests. It is noted that the numerical model was not recalibrated for the comparison with the revetment tests.

This time-averaged model is very efficient computationally and can be applied to design the geometry of a submerged breakwater and examine its performance under various incident wave and water level conditions (Kobayashi et al. 2003). The model will be extended to the porous region landward of the still water shoreline in order to predict the mean and standard deviation of the shoreline oscillation. The extended model will also be applied to predict the stone movement on porous structures and the profile evolutions of cobble and gravel beaches. This relatively simple model may also eventually be extended to assess the effect of a porous structure on long-term beach profile changes.

REFERENCES

Ahrens, J.P. (1989). "Stability of reef breakwaters." *J. Waterw., Port, Coastal, Ocean Eng.*, 115(2), 221 – 234.

Ahrens, J.P., and Ward, D.L. (1991). "Performance of bermed revetments." *J. Waterw. Port, Coastal, Ocean Eng.*, 117(5), 534-540.

Allan, J.C., and Komar, P.D. (2002). "A dynamic revetment and artificial dune for shore protection." *Coastal Engineering 2002, Proc. 28th Coastal Engineering Conf.*, World Scientific, Singapore, 2044-2056.

Artificial reef design manual. (1992). Coastal Branch, River Division, Ministry of Construction, Tokyo, Japan (in Japanese).

Battjes, J.A., and Janssen, J.P.F.M. (1978). "Energy loss and set-up due to breaking of random waves." *Coastal Engineering 1978, Proc. 16th Coastal Engineering Conf.*, ASCE, New York, 569 – 587.

Battjes, J.A., and Stive, M.J.F. (1985). "Calibration and verification of a dissipation model for random breaking waves." *J. Geophys. Res.*, 90(C5), 9159 – 9167.

Clarke, S., Dodd, N., and Damgaard, J. (2004). "Modeling flow in and above a porous beach." *J. Waterw., Port, Coastal, Ocean Eng.*, 130(5), 223 – 233.

Cox, D.T. and Kobayashi, N. (1997). "A kinematic undertow model with a logarithmic boundary layer." *J. Waterw., Port, Coastal, Ocean Eng.*, 123(6), 354 – 360.

Cruz, E.C., Isobe, M., and Watanabe, A. (1992). "Nonlinear wave transformation over a submerged permeable breakwater." *Coastal Engineering 1992, Proc. 23rd Coastal Engineering Conf.*, ASCE, New York, 1101 – 1114.

Kobayashi, N., Cox, D.T., and Wurjanto, A. (1990). "Irregular wave reflection and run-up on rough impermeable slopes." *J. Waterw., Port, Coastal, Ocean Eng.*, 116(6), 708 – 726.

Kobayashi, N., and Johnson, B.D. (1998). "Computer program CSHORE for predicting cross-shore transformation of irregular breaking waves." *Research Rep. No. CACR-98-04*, Center for Applied Coastal Research, Univ. of Delaware, Newark, Del.

Kobayashi, N., Herrman, M.N., Johnson, B.D., and Orzech, M.D. (1998). "Probability distribution of surface elevation in surf and swash zones." *J. Waterw., Port, Coastal, Ocean Eng.*, 124(3), 99 – 107.

Kobayashi, N., Meigs, L.E., Ota, T., and Melby, J.A. (2004). "Irregular breaking wave transmission over submerged porous breakwater." *J. Waterw., Port, Coastal, Ocean Eng.* (submitted).

Kobayashi, N., Pozueta, B., and Melby, J.A. (2003). "Performance of coastal structures against sequences of hurricanes." *J. Waterw., Port, Coastal, Ocean Eng.*, 129(5), 219 – 228.

Kobayashi, N., and Wurjanto, A. (1989). "Wave transmission over submerged breakwaters." *J. Waterw., Port, Coastal and Ocean Eng.*, 115(5), 662 – 680.

Kobayashi, N., and Wurjanto, A. (1990). "Numerical model for waves on rough permeable slopes." *J. Coastal Res.*, SI(7), 149 – 166.

Liu, P.L.-F., Lin, P., Chang, K.-A., and Sakakiyama, T. (1999). "Numerical modeling of wave interaction with porous structures." *J. Waterw., Port, Coastal, Ocean Eng.*, 125(6), 322 – 330.

Madsen, O.S., and White, S.M. (1975). "Reflection and transmission characteristics of porous rubble-mound breakwaters." *Tech. Rep. No. 107*, R.M. Parsons Lab., Mass. Inst. of Tech., Cambridge, Mass.

Meigs, L.E., Kobayashi, N., and Melby, J.A. (2004). "Cobble beaches and revetments." *Coastal Engineering 2004, Proc. 29th Coastal Engineering Conf.*, World Scientific, Singapore (will be published).

Méndez, F.J., Losada, I.J., and Losada, M.A. (2001). "Wave-induced mean magnitudes in permeable submerged breakwaters." *J. Waterw., Port, Coastal, Ocean Eng.*, 127(1), 7 – 15.

Raubenheimer, B., Guza, R.T., and Elgar, S. (1996). "Wave transformation across the inner surf zone." *J. Geophys. Res.*, 101(C10), 25,589 – 25,597.

Sigurdarson, S., Viggosson, G., Tørum, A., and Smarason, O.B. (2001). "Stable berm breakwaters." *Proc. Advanced Design of Maritime Structures in 21st Century*, Port and Harbour Res. Inst., Yokosuka, Japan, 152-159.

Svendsen, I.A., Qin, W., and Ebersole, B.A. (2003). "Modelling waves and currents at the LSTF and other laboratory facilities." *Coastal Eng.*, 50, 19 – 45.

van der Meer, J.W., and Daemen, I.F.R. (1994). "Stability and wave transmission at low-crested rubble mound structures." *J. Waterw., Port, Coastal, Ocean Eng.*, 120(1), 1 – 19.

van Gent, M.R.A. (1994). "The modelling of wave action on and in coastal structures." *Coastal Eng.*, 22, 311 – 339.

van Gent, M.R.A. (1995). "Porous flow through rubble-mound material." *J. Waterw., Port, Coastal, Ocean Eng.*, 121(3), 176 – 181.

Wurjanto, A., and Kobayashi, N. (1993). "Irregular wave reflection and runup on permeable slopes." *J. Waterw., Port, Coastal, Ocean Eng.*, 119(5), 537 – 557.